

Refinement on non-hydrostatic shallow granular flow model in a global Cartesian coordinate system

L. Yuan¹  · W. Liu¹ · J. Zhai¹ · S. F. Wu² · A. K. Patra³ · E. B. Pitman⁴

Received: 24 October 2016 / Accepted: 7 June 2017
© Springer International Publishing AG 2017

Abstract Current shallow granular flow models suited to arbitrary topography can be divided into two types, those formulated in bed-fitted curvilinear coordinates and those formulated in global Cartesian coordinates. The shallow granular flow model of Denlinger and Iverson (J. Geophys. Res. **109**, F01014, 2004) and the Boussinesq-type shallow granular flow theory of Castro-Orgaz et al. (2014) are formulated in a Cartesian coordinate system (with z vertical),

and both account for the effect of nonzero vertical acceleration on depth-averaged momentum fluxes and stress states. In this paper, we first reformulate the vertical normal stress of Castro-Orgaz et al. (2014) in a quadratic polynomial in the relative elevation η . This form allows for analytical depth integration of the vertical normal stress. We then calculate the basal normal stress based on the basal friction law and scaling analysis. These calculations, plus certain constitutive relations, lead to a refined full non-hydrostatic shallow granular flow model, which is further rewritten in a form of Boussinesq-type water wave equations for future numerical studies. In the present numerical study, we apply the open-source code TITAN2D for numerical solution of a low-order version of the full model involving only a mean vertical acceleration correction term. To cure the numerical instability related with discretization of the enhanced gravity, we propose an approximate formula for the enhanced gravity by utilizing the hydrostatic pressure assumption in the bed normal direction. Numerical calculations are conducted for several test cases involving steep slopes. Comparison with a bed-fitted model shows that even the simplified non-hydrostatic Cartesian model can be used to simulate shallow granular flows over arbitrary topography.

✉ L. Yuan
lyuan@lsec.cc.ac.cn

W. Liu
liuwei@lsec.cc.ac.cn

J. Zhai
zhaijian@lsec.cc.ac.cn

S. F. Wu
fengtree@126.com

A. K. Patra
abani@eng.buffalo.edu

E. B. Pitman
pitman@buffalo.edu

¹ LSEC and Institute of Computational Mathematics and Scientific/Engineering Computing, Academy of Mathematics and Systems Science, University of Chinese Academy of Sciences, Chinese Academy of Sciences, Beijing 100190, China

² Department of Computer Science, Guangdong Polytechnic Normal University, Guangzhou 510665, China

³ Department of Mechanical and Aerospace Engineering, University at Buffalo SUNY, Buffalo, NY 14260, USA

⁴ Department of Mathematics, University at Buffalo SUNY, Buffalo, NY 14260, USA

Keywords Granular flow · Depth average · Cartesian coordinate · Arbitrary topography · Non-hydrostatic pressure · Basal normal stress

1 Introduction

Reliable prediction of gravity-driven geophysical mass movements like landslides, debris flows, and rock avalanches can be an invaluable tool in assessing hazard risks and planning strategies for hazard mitigation. It is widely

recognized that the basic ingredients in geophysical mass movements in natural hazards are granular materials, a collection of a larger number of discrete solid particles with interstices filled with a fluid or gas [3]; thus, granular avalanche flows constitute a fundamental case. The relative simplicity of this case makes it an attractive object for developing and testing various predictive models [1].

During a granular avalanche, granular materials slide and flow over topographies and may travel very long distances. The characteristic length in the flowing direction is generally much larger than that in the normal-to-bed direction, e.g., the avalanche thickness. Such a shallowness argument, which originated in the derivation of Saint-Venant equations for modeling shallow water flows, has been widely used in the derivation of continuum flow models for granular avalanches. Earlier shallow granular flow models were formulated by direct analogy with the shallow water equations [4]. Later, Savage and Hutter [5] introduced a depth-integrated theory obeying Coulomb-type yield by which the rapid flow of a finite mass of granular material down a plane slope could be analyzed. Their shallow granular flow model is called the Savage-Hutter (SH) equations. Over the past three decades there has been great progress in shallow granular flow models. The developed models have been shown to be able to reproduce the basic features of both experimental dense granular flows along inclined planes with appropriate constitutive relations [6–12], and some of which have been used to simulate real avalanche flows over natural terrains [13–15].

In describing debris flows over natural terrains, some researchers [16, 17] used the Saint-Venant equations that is referenced in horizontal Cartesian coordinates with a hydrostatic basal pressure of ρgh (where ρ is the bulk density, h is the vertical flow depth, and g is the gravity of the Earth). However, such global Cartesian formulations are only applicable to topography with small slopes because the usual hypothesis of hydrostatic pressure in the vertical direction in the shallow water equations is no longer valid for steep terrain even if it is admissible in the normal-to-bed direction. A few studies [18, 19] directly used formulations in a local Cartesian coordinate system in cell-by-cell way to compute granular flows over natural terrains. However, such a numerical approach is problematic in aligning velocity variables and balancing numerical fluxes of conserved variables between adjacent cells on curved bed as remarked by Denlinger and Iverson [1]. A more elaborate work was to correct both acceleration and friction terms in the Saint-Venant equations in Cartesian coordinates for large slope gradients [20]. Nevertheless, the corrections are based on mechanical considerations rather than mathematical derivations. On the other hand, the SH theory has been generalized rigorously in general curvilinear coordinate systems to describe granular avalanches over general terrains [14, 21, 22]. Although the

bed-fitted formulations are more accurate, they are complicated and need non-trivial grid generation on natural terrains for numerical solution. In order to develop viable shallow water/granular flow models suitable for a general topography, Refs. [23, 24] derived a form of shallow water/granular flow equations that is referenced to a fixed global Cartesian coordinate system but uses thickness in the direction normal to the topography and a parameterized Cartesian velocity field as solution variables. The equations [24] take into account the curvature tensor with all its components and the Coulomb basal friction while ignoring the internal friction effects. Numerical solution using this model has been carried out for a landslide over general terrains [15].

For modeling gravity-driven granular avalanche flows across irregular terrains, Denlinger and Iverson [1] developed depth-averaged governing equations in a global Cartesian coordinate system (with z vertical) that account explicitly for the effect of nonzero vertical accelerations on depth-averaged momentum fluxes and stress states. They used stress transformation between the bed-fitted local Cartesian and the horizontal global Cartesian coordinate systems to get the Coulomb stress states independent of the orientation of the coordinate system. While this model provides familiar conservative fluxes suitable for a finite volume method, the source terms containing the internal stresses are calculated with the otherwise finite element method, and this will introduce extra work.

More recently, Castro-Orgaz et al. [2] developed a non-hydrostatic depth-averaged granular flow theory in the global horizontal-vertical Cartesian coordinate system by making use of the non-hydrostatic Boussinesq-type water wave theory widely used in water wave field (e.g., [25]). In their theory, the effect of vertical motion is taken into account rigorously, and the vertical velocity, vertical acceleration, and vertical normal stresses are determined mathematically using mass and momentum conservation equations without any ad hoc simplification. Some basic features of this theory were explored and analytical solutions of simplified flow cases were obtained, and numerical approaches for treating the additional dispersive terms in the fluxes of the depth-averaged momentum equations were outlined [2]. In almost the same time, Ref. [26] also derived a non-hydrostatic shallow water-type model by a minimal energy constraint and depth-averaging process of the Euler or Navier-Stokes system, and the model is similar to the non-hydrostatic shallow granular flow theory [2] in a sense that the non-hydrostatic part of the pressure will be determined using additional differential equations.

In this paper, we further develop the non-hydrostatic depth-averaged granular flow theory [2]. First, we reformulate the vertical normal stress [2] in a polynomial form in the relative elevation $\eta = z - b(x, y, t)$ (b is the topography). The resulting quadratic form is convenient for analytical

depth integration, and it also reveals the difference between the model [1] and the theory [2]. Second, we compute the basal traction vector from the Coulomb friction law as Refs. [27, 28] did. In this step, we find the vertical component of the basal traction vector is linked to the integration of the z -momentum equation such that an accurate expression for the basal normal stress in terms of the enhanced gravity can be obtained under some scaling arguments. With the above two revisions, a refined complete non-hydrostatic shallow granular flow model is obtained under certain constitutive relations, in which the earth pressure coefficient notation for the lateral normal stresses in soil mechanics and the relation between the lateral shear and normal stresses [8] are adopted. These relations can be replaced or improved in future work. The resultant full model is further rewritten in a form of Boussinesq-type water wave equations presumedly more suitable for implementing available numerical methods developed by the water wave community.

Since the present full non-hydrostatic shallow granular flow equations are still complicated, we only carry out numerical solution of its low-order version, which is similar to the differential form of the model [1]. We implement the lower order model in the open-source shallow granular flow simulation code TITAN2D [29]. In the process, we encountered a numerical instability problem caused by discretizing $\partial \bar{w} / \partial t$ in the enhanced gravity defined as $g' = g + D\bar{w}/Dt$. To overcome this problem, we derive an approximate formula for g' by using the hypothesis of hydrostatic pressure in the bed normal direction and the Taylor expansion. This formula takes into account the effects of bed slope, basal friction, and variation of flow height, and is found to be numerically more stable than the original enhanced gravity. In addition, a more delicate “centripetal normal stress” by using the curvature tensor [11, 24] is added to the basal normal stress in the basal friction and bed slope terms. The resultant simplified non-hydrostatic model is implemented in TITAN2D and tested in several numerical examples. Numerical comparisons with analytical solutions and bed-fitted model show a satisfactory agreement.

2 A survey of two non-hydrostatic models

For later reference in this paper, we briefly review the basic equations of granular avalanche motions and the shallow granular flow equations of Denlinger and Iverson [1] and of Castro-Orgaz et al. [2], respectively.

2.1 Conservation equations

In a horizontal-vertical Cartesian coordinate system where the z direction is opposite to the gravitational acceleration vector \mathbf{g} (Fig. 1), the motion of a fluidized granular mass

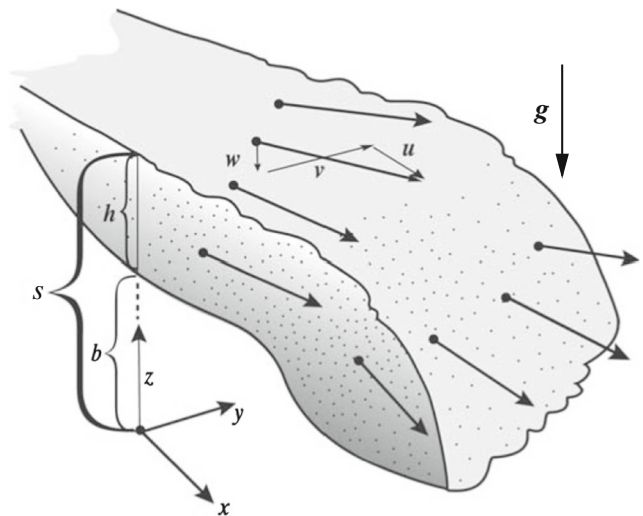


Fig. 1 Sketch illustrating the global coordinate system and variables used to calculate avalanche motion (courtesy of Denlinger and Iverson [1])

is described with the mass and momentum conservation equations

$$\text{div } \mathbf{v} = 0, \tag{1}$$

$$\rho \left[\frac{\partial \mathbf{v}}{\partial t} + \text{div} (\mathbf{v} \otimes \mathbf{v}) \right] = -\text{div } \boldsymbol{\tau} + \rho \mathbf{g}, \tag{2}$$

where t is the time, ρ is the bulk density of the granular mass assumed to be constant in this paper, $\mathbf{v}(x, y, z, t) = (u(x, y, z, t), v(x, y, z, t), w(x, y, z, t))$ denotes the three-dimensional velocity vector inside the avalanche, \otimes is the tensor (or dyadic) product, $\boldsymbol{\tau}(x, y, z, t)$ is the negative Cauchy stress tensor.

Kinematic boundary conditions are imposed on the free surface $z = s(x, y, t)$ and the basal surface $z = b(x, y, t)$, that specify that mass neither enters nor leaves at the free surface or at the base:

$$\left(\frac{\partial s}{\partial t} + u \frac{\partial s}{\partial x} + v \frac{\partial s}{\partial y} - w \right) \Big|_{z=s} = 0, \tag{3}$$

$$\left(\frac{\partial b}{\partial t} + u \frac{\partial b}{\partial x} + v \frac{\partial b}{\partial y} - w \right) \Big|_{z=b} = 0. \tag{4}$$

The dynamic boundary conditions include a traction-free boundary condition at the free surface, and a Coulomb sliding friction law at the basal surface [27]:

$$\boldsymbol{\tau}_s \cdot \mathbf{n}_s = \mathbf{0}, \tag{5}$$

$$\boldsymbol{\tau}_b \cdot \mathbf{n}_b = \frac{\mathbf{v}_r}{|\mathbf{v}_r|} \tan \phi_{\text{bed}} (\mathbf{n}_b \cdot \boldsymbol{\tau}_b \cdot \mathbf{n}_b) + \mathbf{n}_b (\mathbf{n}_b \cdot \boldsymbol{\tau}_b \cdot \mathbf{n}_b), \tag{6}$$

where the outward unit normals (pointing to the outside of the granular mass) are defined as $\mathbf{n}_s = (-\partial_x s, -\partial_y s, 1) / \sqrt{1 + (\partial_x s)^2 + (\partial_y s)^2}$ and $\mathbf{n}_b = (\partial_x b, \partial_y b, -1) / \sqrt{1 + (\partial_x b)^2 + (\partial_y b)^2}$, respectively, ϕ_{bed} is the basal angle of friction and $\mathbf{v}_r = \mathbf{v}_{b+} - \mathbf{v}_{b-}$ is the velocity difference

(satisfying $\mathbf{v}_r \cdot \mathbf{n}_b = 0$) between the fluid on the upper side of the basal surface, \mathbf{v}_{b+} , and the basal topography on the lower side of the interface, \mathbf{v}_{b-} . The factor $\mathbf{v}_r/|\mathbf{v}_r|$ ensures that the Coulomb friction opposes the avalanche motion. For a fixed bed, $\mathbf{v}_{b-} = 0$.

2.2 Shallow granular flow model of Denlinger and Iverson (2004) [1]

Denlinger and Iverson [1] derived a depth-averaged granular flow model in the global Cartesian coordinate system as shown in Fig. 1. They started from conservation Eqs. 1–2 and boundary conditions (3)–(5) and noted that the length scale for avalanche thickness in the z direction is H , whereas the length scale for typical planimetric zone of the avalanche in the x and y directions is L . They assumed

$H \ll L$ typically so that the parameter $\varepsilon = H/L$ is much less than unity. By scaling considerations and integration of the z -component momentum equation across the avalanche thickness with a stress-free condition $\tau_{zz}(s) = 0$ at the free surface, they obtained the vertical normal stress $\tau_{zz}(b)$ at the bed in terms of a hydrostatic pressure plus a depth-averaged vertical acceleration correction term. Then, they assumed that $\tau_{zz}(z)$ varies linearly from $\tau_{zz}(b)$ at the basal surface to 0 at the free surface and that the lateral normal stresses τ_{xx} and τ_{yy} are proportional to τ_{zz} , and assumed a constant velocity profile for the horizontal velocity components (u, v) across the vertical thickness. With these assumptions, they derived following depth-averaged mass and horizontal momentum equations (we correct the signs and the bed slope term typos in [1] in the right-hand side (RHS) of Eqs. 8 and 9)

$$\int_A \left[\frac{\partial h}{\partial t} + \frac{\partial(h\bar{u})}{\partial x} + \frac{\partial(h\bar{v})}{\partial y} \right] dA = 0, \tag{7}$$

$$\int_A \left[\frac{\partial(h\bar{u})}{\partial t} + \frac{\partial}{\partial x} \left(h\bar{u}^2 + \frac{1}{2}k_x g' h^2 \right) + \frac{\partial(h\bar{u}\bar{v})}{\partial y} \right] dA = - \int_A k_x g' h \frac{\partial b}{\partial x} dA - \int_V \frac{\partial \tau_{yx}}{\partial y} dV + \int_A \tau_{zx}(b) dA, \tag{8}$$

$$\int_A \left[\frac{\partial(h\bar{v})}{\partial t} + \frac{\partial(h\bar{u}\bar{v})}{\partial x} + \frac{\partial}{\partial y} \left(h\bar{v}^2 + \frac{1}{2}k_y g' h^2 \right) \right] dA = - \int_A k_y g' h \frac{\partial b}{\partial y} dA - \int_V \frac{\partial \tau_{xy}}{\partial x} dV + \int_A \tau_{zy}(b) dA, \tag{9}$$

where V is an arbitrary control volume, A is its projected area on the horizontal Oxy plane, $h = s - b$ is the flow thickness, measured vertically from the bed at $z = b$ to the free surface at $z = s$, \bar{u}, \bar{v} and \bar{w} are velocity components in the x, y , and z directions, averaged over the vertical thickness h like $\bar{u} = \int_b^s u dz/h$, $k_x = \tau_{xx}/\tau_{zz}$ and $k_y = \tau_{yy}/\tau_{zz}$ are lateral normal stress coefficients that have values directly derived from Coulomb stress calculations and are independent of the orientation of the coordinate system, τ_{ij} are Cartesian components of the stress tensor, and g' is the “total vertical acceleration” [1] (we adopt the term “enhanced gravity” [2] as additional terms due to the vertical acceleration are not included in g') defined by

$$g' \equiv g + \frac{D\bar{w}}{Dt}, \tag{10}$$

$$\frac{D\bar{w}}{Dt} \equiv \frac{\partial \bar{w}}{\partial t} + \bar{u} \frac{\partial \bar{w}}{\partial x} + \bar{v} \frac{\partial \bar{w}}{\partial y}, \tag{11}$$

$$\bar{w} = \frac{1}{2} (w_s + w_b) = \left(\frac{\partial b}{\partial t} + \bar{u} \frac{\partial b}{\partial x} + \bar{v} \frac{\partial b}{\partial y} \right) + \frac{1}{2} \left(\frac{\partial h}{\partial t} + \bar{u} \frac{\partial h}{\partial x} + \bar{v} \frac{\partial h}{\partial y} \right). \tag{12}$$

The governing Eqs. 7–9 are closed by Eqs. 10–12. Denlinger and Iverson [1] solved the equations with finite volume methods using stresses from the previous time step in the RHS source terms. Once a flow solution was obtained, a finite element method was used to calculate internal stresses with dynamic boundary conditions (5)–(6) and to modify these source terms for the next time step.

We will show in Section 3.1 that the differential form of Eqs. 7–9 plus (10)–(12) is a low-order version of a full model refined from the following non-hydrostatic shallow granular flow theory [2]. And a substitute for g' seems to be necessary for curing the numerical instability in discretizing Eq. 10.

2.3 Non-hydrostatic shallow granular flow theory of Castro-Orgaz (2014) [2]

Castro-Orgaz et al. [2] derived a non-hydrostatic Boussinesq-type gravity wave theory for granular media in the same Cartesian coordinate system as shown in Fig. 1. They adopted the same assumptions of shallowness for the vertical depth and constant velocity profile for the

horizontal velocity components (u, v) across the vertical thickness [1]. Starting from Eqs. 1–5, they derived the following governing equations

$$\frac{\partial h}{\partial t} + \frac{\partial(h\bar{u})}{\partial x} + \frac{\partial(h\bar{v})}{\partial y} = 0, \tag{13}$$

$$\begin{aligned} \frac{\partial(h\bar{u})}{\partial t} + \frac{\partial\left(h\bar{u}^2 + \frac{h\bar{\tau}_{xx}}{\rho}\right)}{\partial x} + \frac{\partial\left(h\bar{u}\bar{v} + \frac{h\bar{\tau}_{yx}}{\rho}\right)}{\partial y} \\ = -\frac{1}{\rho}\left(\tau_{xx}\frac{\partial b}{\partial x} + \tau_{yx}\frac{\partial b}{\partial y} - \tau_{zx}\right)_b, \end{aligned} \tag{14}$$

$$\begin{aligned} \frac{\partial(h\bar{v})}{\partial t} + \frac{\partial\left(h\bar{u}\bar{v} + \frac{h\bar{\tau}_{xy}}{\rho}\right)}{\partial x} + \frac{\partial\left(h\bar{v}^2 + \frac{h\bar{\tau}_{yy}}{\rho}\right)}{\partial y} \\ = -\frac{1}{\rho}\left(\tau_{xy}\frac{\partial b}{\partial x} + \tau_{yy}\frac{\partial b}{\partial y} - \tau_{zy}\right)_b, \end{aligned}$$

$$\tau_{zz} = \rho g(h - \eta) + \rho \left[\frac{\partial I}{\partial t} + \nabla \cdot (\bar{\mathbf{u}}I) \right] - \rho w^2, \tag{15}$$

$$w = w_b - (\nabla \cdot \bar{\mathbf{u}})\eta, \tag{16}$$

$$I \equiv \int_z^s w dz = (h - \eta) \frac{\partial b}{\partial t} - \nabla \cdot \left[\frac{(h^2 - \eta^2)}{2} \bar{\mathbf{u}} \right] + h\bar{\mathbf{u}} \cdot \nabla(h + b), \tag{17}$$

where $\eta = z - b$, $\nabla = (\partial_x, \partial_y)$, $\bar{\mathbf{u}} = (\bar{u}, \bar{v})$, and a quantity with bar is the depth-averaged quantity. Note that Eqs. 13, 14 and 15 are the usual depth-averaged mass and horizontal momentum equations. But Eq. 15 results from integration of the z -momentum equation from a generic elevation z to the free surface $z = s$ where a stress-free condition $\tau_{zz}(s) = 0$ is used (the same as [1]), and a constant profile of $\bar{\mathbf{u}}$ across the vertical thickness and negligence of high-order shear stress contributions in Eq. 15 are implied. The vertical velocity component w in (16) results from integration of the continuity Eq. 1 from the bed with the kinematic boundary condition (4) to a generic elevation z . Equation 17 is a definition of I and is calculated from vertical integration of Eq. 16 together with the boundary condition (4).

The system of Eqs. 13–16 are closed if parameterizations of the stress tensor τ are given. Equations 15, 16, and 17 are said to be the core for modeling dispersion effects in depth-averaged models [2]. Castro-Orgaz et al. [2] compared their theory with the Denlinger and Iverson model [1] in 1D steady dry granular flow over a horizontal plane and shown that the latter model introduces a factor (1/4) into the dispersive terms in the momentum flux as compared with the exact factor (1/3) in their full non-hydrostatic shallow granular flow theory. As for numerical solution of the full non-hydrostatic shallow granular flow equations, they mentioned numerical difficulties introduced by dispersion terms and suggested some solution methods developed in water wave simulations.

We remark that integral forms (7)–(9) can be transformed into differential forms (13)–(15) by removing the surface integral, utilizing $\tau_{xx} = k_x \tau_{zz}$, $\tau_{yy} = k_y \tau_{zz}$, $\tau_{zz} = g'(h - \eta)$, and applying Leibnitz’s rule to the second terms in the RHS of Eqs. 8 and 9.

In the following section, we further develop Castro-Orgaz et al.’s theory into a refined full non-hydrostatic shallow granular flow model.

3 Further development of non-hydrostatic shallow granular flow theory

We first reduce the vertical normal stress formula (15) to a polynomial form in the relative elevation η . The result will show that Denlinger and Iverson’s model [1] is a special case of Castro-Orgaz et al.’s theory [2]. Then we calculate the normal stress acting on the bed according to the prescribed friction law. These calculations will lead to a refined full non-hydrostatic shallow granular flow model provided that the required constitutive relations are prescribed. In the end we transform the full model into a form similar to Boussinesq-type water wave equations presumedly more convenient for future numerical studies.

3.1 Simplification of vertical normal stress

The role of $\tau_{zz}(\eta)$ in Eq. (15) is for evaluating $\bar{\tau}_{xx}$, $\bar{\tau}_{yy}$ and $\bar{\tau}_{xy}$, but this form is not convenient for analytical integration in η , so we consider to simplify it. The depth-averaged vertical velocity \bar{w} is computed out from Eq. 16 for use in subsequent derivation,

$$\bar{w} \equiv \frac{1}{h} \int_b^s w dz = w_b - (\nabla \cdot \bar{\mathbf{u}}) \frac{h}{2}. \tag{18}$$

Define $\hat{I} \equiv \int_b^z w dz = \int_b^s w dz - \int_z^s w dz = h\bar{w} - I$, and rewrite Eq. 15 as

$$\begin{aligned} \tau_{zz} = \rho g(h - \eta) + \rho h \left(\frac{\partial \bar{w}}{\partial t} + \bar{\mathbf{u}} \cdot \nabla \bar{w} \right) \\ - \rho \left[\frac{\partial \hat{I}}{\partial t} + \nabla \cdot (\bar{\mathbf{u}} \hat{I}) \right] - \rho w^2, \end{aligned} \tag{19}$$

where the volume conservation Eq. 13 has been used. \hat{I} is computed by inserting (16) into the definition of \hat{I} as

$$\hat{I} = w_b \eta - (\nabla \cdot \bar{\mathbf{u}}) \frac{\eta^2}{2}. \tag{20}$$

Insert (20) into (19), and denote $D/Dt = \partial_t + \bar{\mathbf{u}} \cdot \nabla$, we obtain

$$\begin{aligned}
 \tau_{zz} &= \rho g(h - \eta) + \rho h \frac{D\bar{w}}{Dt} - \rho \left\{ \underbrace{\frac{\partial w_b}{\partial t} \eta}_{\text{to 1}} - \underbrace{w_b \frac{\partial b}{\partial t}}_{\text{to 2}} + (\nabla \cdot \bar{\mathbf{u}}) w_b \eta + \underbrace{\bar{u} \frac{\partial(w_b \eta)}{\partial x} + \bar{v} \frac{\partial(w_b \eta)}{\partial y}}_{\text{expand and to 1 and 2}} \right. \\
 &\quad \left. - \underbrace{\frac{\partial(\nabla \cdot \bar{\mathbf{u}}) \eta^2}{\partial t}}_{\text{to 3}} + \underbrace{(\nabla \cdot \bar{\mathbf{u}}) \eta \frac{\partial b}{\partial t}}_{\text{to 4}} - (\nabla \cdot \bar{\mathbf{u}})^2 \frac{\eta^2}{2} - \underbrace{\frac{\bar{u}}{2} \frac{\partial [(\nabla \cdot \bar{\mathbf{u}}) \eta^2]}{\partial x} - \frac{\bar{v}}{2} \frac{\partial [(\nabla \cdot \bar{\mathbf{u}}) \eta^2]}{\partial y}}_{\text{expand and to 3 and 4}} \right\} \\
 &\quad - \rho w^2 \\
 &= \rho g(h - \eta) + \rho h \frac{D\bar{w}}{Dt} - \rho \left[\underbrace{\frac{Dw_b}{Dt} \eta}_1 - \underbrace{\frac{w_b^2}{2}}_2 - \underbrace{\frac{D(\nabla \cdot \bar{\mathbf{u}}) \eta^2}{Dt}}_3 + \underbrace{(\nabla \cdot \bar{\mathbf{u}}) \eta w_b}_4 \right. \\
 &\quad \left. + (\nabla \cdot \bar{\mathbf{u}}) w_b \eta - (\nabla \cdot \bar{\mathbf{u}})^2 \frac{\eta^2}{2} \right] - \rho w^2 \\
 &= \rho g(h - \eta) + \rho \underbrace{\frac{D\bar{w}}{Dt} (h - \eta)}_{\text{from 1}} - \rho \left[\underbrace{\frac{D(h \nabla \cdot \bar{\mathbf{u}}) \eta}{Dt}}_{\text{from 1 by (18)}} \underbrace{\frac{\eta}{2} \left(-w_b^2 + 2(\nabla \cdot \bar{\mathbf{u}}) w_b \eta - (\nabla \cdot \bar{\mathbf{u}})^2 \eta^2 \right)}_{=-w^2 \text{ by (16)}} \right. \\
 &\quad \left. - \frac{D(\nabla \cdot \bar{\mathbf{u}}) \eta^2}{Dt} \frac{\eta}{2} + (\nabla \cdot \bar{\mathbf{u}})^2 \frac{\eta^2}{2} \right] - \rho w^2 \\
 &= \underbrace{\rho g(h - \eta)}_{\text{hydrostatic}} + \underbrace{\rho \frac{D\bar{w}}{Dt} (h - \eta)}_{\text{mean acceleration}} - \underbrace{\frac{\rho}{2} \left[\frac{D(h \nabla \cdot \bar{\mathbf{u}}) \eta}{Dt} \eta - \frac{D(\nabla \cdot \bar{\mathbf{u}}) \eta^2}{Dt} \eta^2 + (\nabla \cdot \bar{\mathbf{u}})^2 \eta^2 \right]}_{\text{high-order acceleration correction}}. \tag{21}
 \end{aligned}$$

It is seen that τ_{zz} equals to a hydrostatic pressure of the order of ρgH plus a mean vertical acceleration correction term of the order of ρgH and a high-order acceleration correction term of the order of $\rho gH\epsilon$. The last term is parabolic in η and becomes zero at both the basal surface $\eta = 0$ and the free surface $\eta = h$. Note that the first two terms are the same linear distribution of τ_{zz} as in [1]. Further, the depth-averaged vertical velocity (18) is identical to the arithmetic average of vertical velocities at the basal and free surfaces, Eq. 12. Therefore, the first two terms are completely identical to Denlinger and Iverson’s $\tau_{zz}(z)$. The difference between model [1] and model [2] lies in that the latter has a high-order acceleration correction term in Eq. 21.

3.2 Basal traction vector calculation

Noting that the outward unit vector normal to the bed is $\mathbf{n}_b = (\partial_x b, \partial_y b, -1)/\Delta_b$, where $\Delta_b = [1 + (\partial b/\partial x)^2 + (\partial b/\partial y)^2]^{1/2}$ is the normalization factor, the basal traction vector $\mathbf{T} = (T_x, T_y, T_z) = \boldsymbol{\tau}_b \cdot \mathbf{n}_b$ can be written as

$$\boldsymbol{\tau}_b \cdot \mathbf{n}_b = \frac{1}{\Delta_b} \begin{pmatrix} \tau_{xx} \frac{\partial b}{\partial x} + \tau_{yx} \frac{\partial b}{\partial y} - \tau_{zx} \\ \tau_{xy} \frac{\partial b}{\partial x} + \tau_{yy} \frac{\partial b}{\partial y} - \tau_{zy} \\ \tau_{xz} \frac{\partial b}{\partial x} + \tau_{yz} \frac{\partial b}{\partial y} - \tau_{zz} \end{pmatrix}_b. \tag{22}$$

As noted in Refs. [27, 28], the RHS terms in Eqs. 14 and 15 are horizontal components of the basal traction vector. The vertical component of the basal traction vector appears in the integration of the z -component equation of (2) from $z = b$ to $z = s$ by using Leibnitz’s rule and boundary conditions (3), (4), and (5),

$$\left(\tau_{zz} - \tau_{xz} \frac{\partial b}{\partial x} - \tau_{yz} \frac{\partial b}{\partial y}\right)_b = \rho g h + \rho \left[\frac{\partial}{\partial t} \int_b^s w dz + \frac{\partial}{\partial x} \int_b^s u w dz + \frac{\partial}{\partial y} \int_b^s v w dz \right] + \frac{\partial}{\partial x} \int_b^s \tau_{xz} dz + \frac{\partial}{\partial y} \int_b^s \tau_{yz} dz. \tag{23}$$

With the assumption of constant profile for u and v , Eq. 23 becomes

$$\left(\tau_{zz} - \tau_{xz} \frac{\partial b}{\partial x} - \tau_{yz} \frac{\partial b}{\partial y}\right)_b = \rho g h + \rho h \frac{D\bar{w}}{Dt} + \frac{\partial(h\bar{\tau}_{xz})}{\partial x} + \frac{\partial(h\bar{\tau}_{yz})}{\partial y}. \tag{24}$$

If $\tau_{zz}|_b$, $\tau_{xz}|_b$, $\tau_{yz}|_b$, $\bar{\tau}_{xz}$ and $\bar{\tau}_{yz}$ are $\mathcal{O}(\rho g H)$, \bar{u} , \bar{v} , and \bar{w} are $\mathcal{O}(\sqrt{gL})$, t is $\mathcal{O}(\sqrt{L/g})$, and $\partial b/\partial x$ and $\partial b/\partial y$ are $\mathcal{O}(1)$, then only the last two terms in the RHS in Eq. 24 are $\mathcal{O}(\rho g H \varepsilon)$, while all other terms are $\mathcal{O}(\rho g H)$. Therefore, the last two terms in the RHS in Eq. 24 can be neglected and the equation becomes

$$\left(\tau_{zz} - \tau_{xz} \frac{\partial b}{\partial x} - \tau_{yz} \frac{\partial b}{\partial y}\right)_b = \rho h \left(g + \frac{D\bar{w}}{Dt}\right) = \rho g' h. \tag{25}$$

Multiply the Coulomb friction law (6) with Δ_b and expand the three components in the x , y and z directions, respectively,

$$\left(\tau_{xx} \frac{\partial b}{\partial x} + \tau_{yx} \frac{\partial b}{\partial y} - \tau_{zx}\right)_b = (\mathbf{n}_b \cdot \boldsymbol{\tau}_b \cdot \mathbf{n}_b) \left[\frac{\Delta_b u_r}{|\mathbf{v}_r|} \tan \phi_{bed} + \frac{\partial b}{\partial x} \right], \tag{26}$$

$$\left(\tau_{xy} \frac{\partial b}{\partial x} + \tau_{yy} \frac{\partial b}{\partial y} - \tau_{zy}\right)_b = (\mathbf{n}_b \cdot \boldsymbol{\tau}_b \cdot \mathbf{n}_b) \left[\frac{\Delta_b v_r}{|\mathbf{v}_r|} \tan \phi_{bed} + \frac{\partial b}{\partial y} \right], \tag{27}$$

$$\left(\tau_{xz} \frac{\partial b}{\partial x} + \tau_{yz} \frac{\partial b}{\partial y} - \tau_{zz}\right)_b = (\mathbf{n}_b \cdot \boldsymbol{\tau}_b \cdot \mathbf{n}_b) \left[\frac{\Delta_b w_r}{|\mathbf{v}_r|} \tan \phi_{bed} - 1 \right], \tag{28}$$

where $\mathbf{n}_b \cdot \boldsymbol{\tau}_b \cdot \mathbf{n}_b = \mathbf{n}_b \cdot \mathbf{T}$ is the normal stress acting on the basal surface in the outward normal direction, and $\mathbf{v}_r = (u_r, v_r, w_r)$ is the (tangential) velocity difference at the bed. By combining Eq. (28) with Eq. (25), we obtain the bed normal stress

$$\mathbf{n}_b \cdot \boldsymbol{\tau}_b \cdot \mathbf{n}_b = \frac{\rho g' h}{1 - \frac{\Delta_b w_r}{|\mathbf{v}_r|} \tan \phi_{bed}} = \beta \rho g' h, \tag{29}$$

where

$$\beta = \frac{1}{1 - \frac{\Delta_b w_r}{|\mathbf{v}_r|} \tan \phi_{bed}}. \tag{30}$$

Consequently, the horizontal components of the basal traction vector in Eqs. 26 and 27 are

$$\begin{aligned} \left(\tau_{xx} \frac{\partial b}{\partial x} + \tau_{yx} \frac{\partial b}{\partial y} - \tau_{zx}\right)_b &= \beta \rho g' h \left(\frac{\Delta_b u_r}{|\mathbf{v}_r|} \tan \phi_{bed} + \frac{\partial b}{\partial x} \right), \\ \left(\tau_{xy} \frac{\partial b}{\partial x} + \tau_{yy} \frac{\partial b}{\partial y} - \tau_{zy}\right)_b &= \beta \rho g' h \left(\frac{\Delta_b v_r}{|\mathbf{v}_r|} \tan \phi_{bed} + \frac{\partial b}{\partial y} \right). \end{aligned} \tag{31}$$

We remark that the normal stress acting on the bed can also be calculated directly from expansion of $\mathbf{n}_b \cdot \boldsymbol{\tau}_b \cdot \mathbf{n}_b$ rather than from Eq. 29 as long as a constitutive equation and a velocity profile in z are given. In cases when a basal friction law (Coulomb, Manning) is given, the use of Eq. 29 for calculating the basal normal stress is natural and simpler.

3.3 A refined full non-hydrostatic shallow granular flow model

To close Eqs. 14 and 15, lateral normal and shear stresses, τ_{xx} , τ_{yy} , τ_{xy} and τ_{yx} have to be parameterized. Savage and Hutter [5] proposed to use the Mohr-Coulomb soil constitutive law for the avalanche materials in the shallow-water continuum model, in which the lateral shear stresses τ_{xy} and τ_{yx} are omitted, and the lateral normal stresses τ_{xx} and τ_{yy} are related to the normal stress τ_{zz} in the depth direction in standard fashion through the earth pressure coefficients k_x and k_y respectively. However, the method of determining k_x and k_y [5, 7, 30] assumes that two principal axes of the stress tensor are in the x and y directions, This *ad hoc* assumption destroys the rotational invariance of the equations about the z direction perpendicular to the tangential plane. To amend this deficit, a variety of models have been proposed [14, 31, 32]. For example, Ref. [33], based on Ref. [31], used a symmetric earth pressure coefficient matrix \mathbf{K} that is diagonalizable by rotating the coordinates with an invertible rotation matrix $\mathbf{T} = \begin{pmatrix} \cos \gamma & -\sin \gamma \\ \sin \gamma & \cos \gamma \end{pmatrix}$ such that

$$\mathbf{K} = \mathbf{T} \begin{pmatrix} k_1 & 0 \\ 0 & k_2 \end{pmatrix} \mathbf{T}^{-1}, \text{ and } \begin{pmatrix} \tau_{xx} & \tau_{xy} \\ \tau_{yx} & \tau_{yy} \end{pmatrix} = \tau_{zz} \mathbf{K}.$$

Here, γ is the angle between the primary principal axis (assumed parallel to the local flow velocity [31]) and the x -axis, and k_1 and k_2 are the primary and secondary

earth pressure coefficients depending on the basal and internal friction angles and the dilation/compaction states in principal axis directions. In this work, we adopt the

isotropic depth averaged lateral normal stresses and a relation between the lateral shear and normal stresses deduced from the Coulomb equation [34],

$$\begin{aligned} \bar{\tau}_{xx} = \bar{\tau}_{yy} = k_{ap} \bar{\tau}_{zz}, \quad k_{ap} = k_x = k_y = 2 \frac{1 \mp \sqrt{1 - \cos^2 \phi_{int} / \cos^2 \phi_{bed}}}{\cos^2 \phi_{int}} - 1, \quad \frac{\partial \bar{u}}{\partial x} + \frac{\partial \bar{v}}{\partial y} \geq 0, \\ \bar{\tau}_{xy} = \bar{\tau}_{yx} = -\text{sgn} \left(\frac{\partial \bar{u}}{\partial y} + \frac{\partial \bar{v}}{\partial x} \right) k_{ap} \bar{\tau}_{zz} \sin \phi_{int} = S \bar{\tau}_{zz}, \end{aligned} \tag{32}$$

where $S = -\text{sgn} \left(\frac{\partial \bar{u}}{\partial y} + \frac{\partial \bar{v}}{\partial x} \right) k_{ap} \sin \phi_{int}$. The argument in the sign function in Eq. 32 is slightly modified from Ref. [34] in order to ensure $\bar{\tau}_{xy} = \bar{\tau}_{yx}$. Equation 32 is rotationally invariant with respect to the z -axis. With these stress relations, the depth-averaged lateral normal and shear stresses $\bar{\tau}_{xx}$, $\bar{\tau}_{yy}$, $\bar{\tau}_{xy}$ and $\bar{\tau}_{yx}$ in momentum Eqs. 14 and 15 only require depth integration of $\tau_{zz}(\eta)$ from Eq. 21, which can be done analytically after denoting $\Phi = \nabla \cdot \bar{\mathbf{u}}$. The basal traction horizontal components in the RHS of Eqs. 14 and 15 are evaluated with Eq. 31. With these terms available and a constant bulk density, we transform Eqs. 13-15 into refined full non-hydrostatic shallow granular flow equations

$$\begin{aligned} \frac{\partial}{\partial t} \begin{bmatrix} h \\ h\bar{u} \\ h\bar{v} \end{bmatrix} + \frac{\partial}{\partial x} \begin{bmatrix} h\bar{u}^2 + k_x \left[\frac{1}{2} g' h^2 + \frac{h^3}{12} \left(\Phi^2 - \frac{D\Phi}{Dt} \right) \right] \\ h\bar{u}\bar{v} + S \left[\frac{1}{2} g' h^2 + \frac{h^3}{12} \left(\Phi^2 - \frac{D\Phi}{Dt} \right) \right] \\ h\bar{v}^2 + k_y \left[\frac{1}{2} g' h^2 + \frac{h^3}{12} \left(\Phi^2 - \frac{D\Phi}{Dt} \right) \right] \end{bmatrix} \\ + \frac{\partial}{\partial y} \begin{bmatrix} h\bar{u}\bar{v} + S \left[\frac{1}{2} g' h^2 + \frac{h^3}{12} \left(\Phi^2 - \frac{D\Phi}{Dt} \right) \right] \\ h\bar{v}^2 + k_y \left[\frac{1}{2} g' h^2 + \frac{h^3}{12} \left(\Phi^2 - \frac{D\Phi}{Dt} \right) \right] \end{bmatrix} \\ = \begin{bmatrix} 0 \\ -\beta g' h \left(\frac{\Delta_b u_r}{|\mathbf{v}_r|} \tan \phi_{bed} + \frac{\partial b}{\partial x} \right) \\ -\beta g' h \left(\frac{\Delta_b v_r}{|\mathbf{v}_r|} \tan \phi_{bed} + \frac{\partial b}{\partial y} \right) \end{bmatrix}, \end{aligned} \tag{33}$$

where the h^3 terms in the depth-averaged vertical normal stress has been simplified by using the volume conservation Eq. 13. System (33) can be further cast into a frequently used form of Boussinesq-type water wave equations (e.g., [35, 36]) as follows. If we absorb time partial derivatives in the convective fluxes into $\partial_t(h\bar{u}, h\bar{v})$ by utilizing Eq. 13 and assuming that k_x, k_y and S can be extracted out of the differential operators, we can obtain (overbars in \bar{u}, \bar{v} and \bar{w} have been omitted in the following context to simplify notations)

$$\frac{\partial \mathbf{U}}{\partial t} + \frac{\partial \mathbf{F}}{\partial x} + \frac{\partial \mathbf{G}}{\partial y} = \mathbf{S}_{f-b} + \mathbf{S}_d, \tag{34}$$

where

$$\mathbf{U} = \begin{bmatrix} h \\ U \\ V \end{bmatrix} = \begin{bmatrix} hu + \frac{k_x}{2} \frac{\partial (h^2 w)}{\partial x} + \frac{S}{2} \frac{\partial (h^2 w)}{\partial y} - \frac{k_x}{12} \frac{\partial (h^3 \Phi)}{\partial x} - \frac{S}{12} \frac{\partial (h^3 \Phi)}{\partial y} \\ hv + \frac{S}{2} \frac{\partial (h^2 w)}{\partial x} + \frac{k_y}{2} \frac{\partial (h^2 w)}{\partial y} - \frac{S}{12} \frac{\partial (h^3 \Phi)}{\partial x} - \frac{k_y}{12} \frac{\partial (h^3 \Phi)}{\partial y} \end{bmatrix}, \tag{35}$$

$$\mathbf{F} = \begin{bmatrix} hu \\ hu^2 + \frac{1}{2} g' h^2 \\ huv \end{bmatrix}, \quad \mathbf{G} = \begin{bmatrix} hv \\ huv \\ hv^2 + \frac{1}{2} g' h^2 \end{bmatrix}, \tag{36}$$

$$\mathbf{S}_{f-b} = \begin{bmatrix} 0 \\ -\beta g' h \left(\frac{\Delta_b u_r}{|\mathbf{v}_r|} \tan \phi_{bed} + \frac{\partial b}{\partial x} \right) \\ -\beta g' h \left(\frac{\Delta_b v_r}{|\mathbf{v}_r|} \tan \phi_{bed} + \frac{\partial b}{\partial y} \right) \end{bmatrix}, \quad \mathbf{S}_d = - \begin{bmatrix} 0 \\ k_x \frac{\partial \Gamma}{\partial x} + S \frac{\partial \Gamma}{\partial y} \\ S \frac{\partial \Gamma}{\partial x} + k_y \frac{\partial \Gamma}{\partial y} \end{bmatrix}, \tag{37}$$

$$\begin{aligned} \Gamma = \frac{1}{2} \left[u \frac{\partial (h^2 w)}{\partial x} + v \frac{\partial (h^2 w)}{\partial y} + 2h^2 w \Phi \right] \\ - \frac{1}{12} \left[u \frac{\partial (h^3 \Phi)}{\partial x} + v \frac{\partial (h^3 \Phi)}{\partial y} + 2h^3 \Phi^2 \right]. \end{aligned} \tag{38}$$

Here, \mathbf{S}_{f-b} are the friction and bed slope terms, and \mathbf{S}_d is the dispersive terms. However, we can see that the lumped conservative variable vector \mathbf{U} and the dispersive terms are complicated, so we leave numerical solution of Eq. 34 to future research. In the remaining parts of this paper, we will focus on numerical solution of a simplified model deduced from system (33).

Here we summarize the assumptions made in deriving the full model (33). The assumptions are (i) shallowness of the vertical depth relative to the horizontal scale of the avalanches, (ii) constant horizontal velocity profiles across the vertical depth, and (iii) some relations between the lateral normal and shear stresses and the vertical normal stress like Eq. 32. From Eq. 33 to the Boussinesq-type Eq. 34, a further assumption that k_x, k_y and S can be extracted out of the differential operators is made. The full model is more suitable for dry granular avalanches over steep terrains and capable of simulating dispersive effects as illustrated for simple 1D cases [2]. The shortcomings of the full model are the mathematical complexity, the need to develop a new numerical method and the resulting large computational cost.

In the simplified model to be given in Section 4, the h^3 terms in Eq. 33 are neglected. Two further assumptions are made: (i) the pressure is hydrostatic in the normal-to-bed direction, and (ii) the variation of the bed slope is small such that the basal surface can be regarded as a plane locally. The two assumptions are utilized to obtain an approximate enhanced gravity to make the reduced model work in the framework of TITAN2D, and they are unnecessary if a stable numerical method is available. Although the simplified model loses some non-hydrostatic effects compared to Eq. 33, it is remedied by accounting for a centripetal force involving the full curvature tensor [11, 24]. Therefore, the simplified model is still more suitable for curved steep terrains than shallow water-like SH equations in the global Cartesian coordinate system with a constant gravity.

4 A simplified non-hydrostatic shallow granular flow model

Our initial simplified non-hydrostatic shallow granular flow model results from system (33) by neglecting all the h^3 terms in the convective fluxes, which is the same as the model [1] except slightly different lateral normal-shear stress relation (32) and basal normal stress (29). However, we encountered numerical instability problem when implementing this initial model (also the model [1]) on TITAN2D [29]. Therefore, we try to find an approximate formula for the enhanced gravity to be given in Section 4.1, and correspondingly, we add a “centripetal normal stress” due to the curvature tensor to the original basal normal stress in the RHS terms. Our final simplified model is presented in Section 4.2.

4.1 Enhanced gravity

In implementing the original enhanced gravity g' (Eq. 10) in TITAN2D, we found that the finite difference approximation for $\partial \bar{w} / \partial t$ often causes numerical instability or irregularity. Therefore, we derive an approximate formula for g' by letting the bed normal stress (29) equal to the traditional hydrostatic bed normal stress obtained from the shallow flow argument in a bed-fitted coordinate system, as described below.

Based on scaling analysis of equations written in a local Cartesian coordinate system with the \tilde{z} axis normal to the bed [5, 27, 34, 37], the bed normal stress balances the normal component of the mass weight if neglecting curvature effects,

$$\mathbf{n}_b \cdot \boldsymbol{\tau}_b \cdot \mathbf{n}_b = \rho g h_n \cos \theta. \tag{39}$$

Here, θ is the angle between the vertical z -axis and the normal to the bed, and h_n is the depth in the bed normal

direction, see Fig. 2. If the variation of the bed slope is small, then the basal surface can be regarded as a planar surface in proximity of position x_s , thus there is a geometrical relation between the vertical depth $h(x_s + \Delta x)$ at $x_s + \Delta x$ and the normal depth h_n at x_s ,

$$h_n = h(x_s + \Delta x) \cos \theta \tag{40}$$

where $\Delta x = h_n \sin \theta$. Using the first order Taylor expansion with respect to position x_s , we obtain

$$h_n \approx \left(h(x_s) + h_n \sin \theta \left. \frac{\partial h}{\partial X} \right|_{x_s} \right) \cos \theta,$$

i.e.,

$$h_n = \frac{h \cos \theta}{1 - \left. \frac{\partial h}{\partial X} \right|_{x_s} \tan \theta \cos^2 \theta}, \tag{41}$$

where $\partial / \partial X = - \left(\partial_x b / \sqrt{(\partial_x b)^2 + (\partial_y b)^2} \right) \partial / \partial x - \left(\partial_y b / \sqrt{(\partial_x b)^2 + (\partial_y b)^2} \right) \partial / \partial y$ is the directional derivative in the horizontal plane in the steepest downslope direction. Note that Eq. 41 takes account for variation of h in space, thus is expected to be more accurate than $h_n = h \cos \theta$ valid for uniform depth as given by Juez et al. [38].

Now, let Eq. 29 equal to Eq. 39 together with Eq. 41. Noting that $\tan \theta = \sqrt{(\partial_x b)^2 + (\partial_y b)^2}$, we obtain an approximate formula for the enhanced gravity

$$g' = \frac{g \left(1 - \frac{\Delta_b w_r}{|\mathbf{v}_r|} \tan \phi_{\text{bed}} \right) \cos^2 \theta}{1 + \left(\frac{\partial h}{\partial x} \frac{\partial b}{\partial x} + \frac{\partial h}{\partial y} \frac{\partial b}{\partial y} \right) \cos^2 \theta}, \tag{42}$$

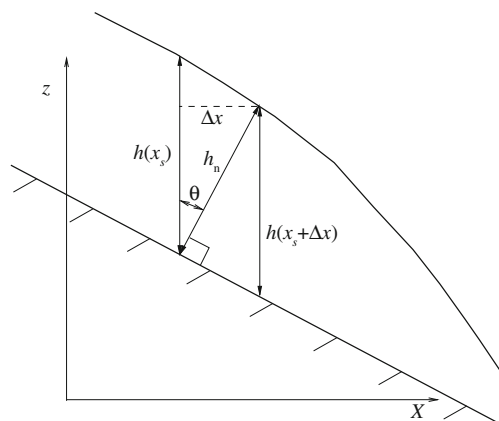


Fig. 2 Relation between vertical and normal depths, where $\Delta x = h_n \sin \theta$, and X is in the horizontally projected steepest downslope direction

which does not involve time derivative occurred in Eq. 10. We find this g' is numerically more stable than Eq. 10 when implemented in TITAN2D. The disadvantage of this g' is that when $\partial h/\partial x$ and $\partial h/\partial y$ are very large near shock waves or initial jumps and the second term in the denominator is negative, the denominator may approach zero during the flow evolution. In our computation, to avoid this problem, a varying under-relaxation factor, $\exp(-\omega|\mathbf{v}_r||\nabla h|)$, is multiplied in front of the second term in the denominator of Eq. 42, where ω is a free parameter (tuned in $1 \sim 3$ in this work). It is seen that when the magnitude of basal velocity difference \mathbf{v}_r or gradient ∇h is large (e.g., supercritical flows with shocks or large initial jumps), this factor becomes small so as to suppress destabilization. On the other hand, when ∇h is small or \mathbf{v}_r approaches 0, this factor becomes 1 so as to recover the original Eq. 42.

The rationale for bed normal stress (29) together with enhanced gravity (42) can be verified by a simple one-dimensional granular flow example of uniform thickness descending a frictionless slope inclined at a constant angle θ [1]. Since $\phi_{\text{bed}} = 0$ and $\partial h/\partial x = 0$, Eq. 42 gives $g' = g \cos^2 \theta$ which is the same as that in [1], and Eq. 29 gives $\mathbf{n}_b \cdot \boldsymbol{\tau}_b \cdot \mathbf{n}_b = \rho gh \cos^2 \theta = \rho gh_n \cos \theta$ which is evidently correct. Another example to verify the correctness of Eqs. 29 and 42 is the 1D static steady state of shallow water flows. For such a state, $h + b = \text{const}$, hence $\partial h/\partial x = -\partial b/\partial x = \tan \theta$, and Eq. 42 gives $g' = g$ so that Eq. 29 recovers the traditional hydrostatic basal pressure ρgh . The present approximate h_n (41) along with Eq. 39 also recovers ρgh . On the other hand, the approximation of $h_n = h \cos \theta$ as in Ref. [38] together with Eq. 39 will lead to a basal pressure of $\rho gh \cos^2 \theta$, which is incorrect for this state.

4.2 Governing equations of the simplified non-hydrostatic model

We restrict ourself to a fixed bed (i.e., $\partial b/\partial t = 0$) in the following context. For the basal friction terms in the RHS of system (33), the basal velocity difference in the basal sliding friction law is $u_r \approx \bar{u}$, $v_r \approx \bar{v}$, and $w_r = w_b = \bar{u}b_x + \bar{v}b_y$, so that $|\mathbf{v}_r| = \sqrt{u_r^2 + v_r^2 + w_r^2} = \sqrt{\bar{u}^2 + \bar{v}^2 + (\bar{u}b_x + \bar{v}b_y)^2}$. It is noted that the approximate enhanced gravity (42) does not reflect the curvature effects of terrains. One important effect of the curvature is to produce an additional friction force linked to centrifugal acceleration. Following Refs. [24] and [11], we account for the curvature effects by adding a centripetal force term involving the curvature tensor \mathcal{H} of the bed profile, $(\mathbf{u}^T \mathcal{H} \mathbf{u})h_n/c^2$, to the basal normal stress ($\beta g'h$) occurring in the RHS of the momentum equations. Here, $c = \cos \theta$, h_n is the avalanche

thickness in the bed normal direction estimated with Eq. 41, and the curvature tensor [11] is

$$\mathcal{H} = c^3 \begin{bmatrix} \frac{\partial^2 b}{\partial x^2} & \frac{\partial^2 b}{\partial x \partial y} \\ \frac{\partial^2 b}{\partial x \partial y} & \frac{\partial^2 b}{\partial y^2} \end{bmatrix}. \tag{43}$$

The final set of governing equations of the simplified non-hydrostatic model result from system (33) by dropping all h^3 terms in the LHS and adding the centrifugal force due to curvature only to the basal normal stress in the RHS. The equations can be written in vector form (overbars in u, v have been omitted for brevity)

$$\frac{\partial \mathbf{U}}{\partial t} + \frac{\partial \mathbf{F}}{\partial x} + \frac{\partial \mathbf{G}}{\partial y} = \mathbf{S}(\mathbf{U}), \tag{44}$$

where

$$\mathbf{U} = \begin{pmatrix} h \\ hu \\ hv \end{pmatrix}, \quad \mathbf{F} = \begin{pmatrix} hu \\ hu^2 + \frac{1}{2}k_x g' h^2 \\ huv \end{pmatrix},$$

$$\mathbf{G} = \begin{pmatrix} hv \\ huv \\ hv^2 + \frac{1}{2}k_y g' h^2 \end{pmatrix}, \quad \mathbf{S}(\mathbf{U}) = \begin{pmatrix} 0 \\ s_x \\ s_y \end{pmatrix}, \tag{45}$$

and

$$s_x = -\frac{S}{2} \frac{\partial(g'h^2)}{\partial y} - \left(\beta g'h + \frac{\mathbf{u}^T \mathcal{H} \mathbf{u}}{c^2} h_n \right)_+ \left(\frac{u}{|\mathbf{v}_r|} \Delta_b \tan \phi_{\text{bed}} + \frac{\partial b}{\partial x} \right),$$

$$s_y = -\frac{S}{2} \frac{\partial(g'h^2)}{\partial x} - \left(\beta g'h + \frac{\mathbf{u}^T \mathcal{H} \mathbf{u}}{c^2} h_n \right)_+ \left(\frac{v}{|\mathbf{v}_r|} \Delta_b \tan \phi_{\text{bed}} + \frac{\partial b}{\partial y} \right). \tag{46}$$

The subscript “+” stands for the positive part, $x_+ = \max(0, x)$, and $\mathbf{u} = (u, v)^T$. Note that the depth-averaged lateral shear stress terms have been placed to the first terms in the RHS of Eq. 46. They could be retained in convective fluxes \mathbf{F} and \mathbf{G} , but we follow Refs. [18, 34] to attribute them to the RHS internal friction source terms. This arrangement makes Eq. 44 look like the traditional shallow water equations in the horizontal-vertical Cartesian coordinate system except a variable g' .

5 Numerical method

5.1 Finite volume method

The governing Eq. 44 is solved with a Godunov type finite volume method for solving hyperbolic conservation laws.

We use a horizontal Cartesian mesh to discretize the computational domain. The flow solution variables (h, hu, hv) are cell averages on each rectangular mesh cell. The finite volume method used is a second-order predictor-corrector Godunov method [39] with van Leer MUSCL reconstruction for \mathbf{U} . The intercell numerical flux is computed with the HLL flux. The wet/dry front is treated by using the Riemann invariant of the wave emanating from the front [8]. The source term \mathbf{S} is evaluated in a pointwise way using cell average values. The predictor-corrector scheme used in open-source code TITAN2D is listed as follows.

Equation 44 can be rewritten as

$$\mathbf{U}_t + \mathbf{A} \cdot \partial_x \mathbf{U} + \mathbf{B} \cdot \partial_y \mathbf{U} = \mathbf{S}(\mathbf{U}), \tag{47}$$

where $\mathbf{A} = (\partial \mathbf{F} / \partial \mathbf{U})_{g'=\text{Const}}$ and $\mathbf{B} = (\partial \mathbf{G} / \partial \mathbf{U})_{g'=\text{Const}}$ are approximate Jacobian matrices of fluxes evaluated with g' frozen at the previous time level, which have familiar forms as in the literature (e.g., [8, 30]).

Given $\mathbf{U}_{i,j}^n$, the (i, j) cell average at time level n , the middle time predictor step is:

$$\mathbf{U}_{i,j}^{n+\frac{1}{2}} = \mathbf{U}_{i,j}^n - \frac{\Delta t}{2} \left(\mathbf{A}_{i,j}^n \Delta_x \mathbf{U}_{i,j}^n + \mathbf{B}_{i,j}^n \Delta_y \mathbf{U}_{i,j}^n - \mathbf{S}_{i,j}^n \right), \tag{48}$$

where Δt is the time step, $\Delta_x \mathbf{U}$ and $\Delta_y \mathbf{U}$ are limited slopes of \mathbf{U} in the x and y directions, respectively. The depth-averaged lateral shear stress terms in \mathbf{S} are expanded using the chain rule, e.g., $\partial(g'h^2)/\partial y = h^2 \partial_y g' + 2g'h \Delta_y h$, and the two partial derivatives are discretized like $\Delta_y \mathbf{U}$.

In the corrector step, a conservation update of \mathbf{U} is computed as follows:

$$\mathbf{U}_{i,j}^{n+1} = \mathbf{U}_{i,j}^n - \frac{\Delta t}{\Delta x} \left(\mathbf{F}_{i+\frac{1}{2}}^{n+\frac{1}{2}} - \mathbf{F}_{i-\frac{1}{2}}^{n+\frac{1}{2}} \right) - \frac{\Delta t}{\Delta y} \left[\mathbf{G}_{j+\frac{1}{2}}^{n+\frac{1}{2}} - \mathbf{G}_{j-\frac{1}{2}}^{n+\frac{1}{2}} \right] + \Delta t \mathbf{S}_{i,j}^{n+\frac{1}{2}}, \tag{49}$$

where $\mathbf{F}_{i+1/2}^{n+1/2} = \mathbf{F}^{\text{HLL}}(\mathbf{U}_{i+1/2}^l, \mathbf{U}_{i+1/2}^r)$, and the left and right state values are obtained by the MUSCL reconstruction of the cell average values to the edge position; that is, $\mathbf{U}_{i+1/2}^l = \mathbf{U}_{i,j}^{n+1/2} + (\Delta x/2) \Delta_x \mathbf{U}_{i,j}^{n+1/2}$, and $\mathbf{U}_{i+1/2}^r = \mathbf{U}_{i+1,j}^{n+1/2} - (\Delta x/2) \Delta_x \mathbf{U}_{i+1,j}^{n+1/2}$. Notice that the mechanical behavior of a Coulomb material has to be taken into account when evaluating the friction force in \mathbf{S} . The frictional force will be treated by a special procedure to be given in Section 5.2.

The above predictor-corrector scheme is implemented in TITAN2D, which has been incorporated with parallel adaptive Cartesian meshes and geographic information system (GIS) databases [18, 29].

5.2 Admissible friction and stopping criteria

The granular material can keep/attain static equilibrium even with an inclined free surface if the tilt angle of the free surface is less than the internal friction angle. This equilibrium state is not automatically preserved by a finite volume scheme discretized from the model solely using the Coulomb friction threshold. Therefore, either a special procedure has to be introduced in the solution process [12, 28] or a “well-balanced”-like numerical scheme has to be constructed to reserve this special steady state at rest [11]. In this paper, we adopt a special procedure. This procedure will invoke a modification to the momentum variables when the magnitude of an admissible tangential stress vector \mathbf{T}_t [12] (or so-called net driving force [28]) is smaller than the Coulomb friction threshold $\tau_{\text{max}} = \beta g'h \tan \phi_{\text{bed}}$. In the following, we describe how to calculate the admissible tangential stress vector \mathbf{T}_t . The calculation is similar to that in Ref. [28]. We take the corrector step (49) as an example. A similar procedure also applies to the predictor step (48).

The mass and momentum components in Eq. 49 for any mesh cell i are

$$\begin{aligned} h_i^{n+1} &= h_i^n + \mathcal{F}_{hi}^{n+\frac{1}{2}}, \\ \mathbf{q}_i^{n+1} &= \mathbf{q}_i^n + \mathcal{F}_{\mathbf{q}i}^{n+\frac{1}{2}} - \Delta t \mathbf{s}_{bi}^{n+\frac{1}{2}} + \Delta t \mathbf{f}_i^{n+\frac{1}{2}}, \end{aligned} \tag{50}$$

where $\mathbf{q} = (hu, hv)$, \mathcal{F} is the flux difference terms, \mathbf{s}_b is the bed slope source term, and $\mathbf{f}_i^{n+1/2}$ is the sum of lateral shear and basal friction terms in Eq. 46, which has to be quantified in the following special procedure. Define

$$\tilde{\mathbf{q}}_i^{n+1} = \mathbf{q}_i^n + \mathcal{F}_{\mathbf{q}i}^{n+1/2} - \Delta t \mathbf{s}_{bi}^{n+\frac{1}{2}}, \tag{51}$$

which is an intermediate solution without the friction terms. $\tilde{\mathbf{q}}_i^{n+1}/\Delta t$ is the horizontal components of the net driving force [28] or the admissible basal shear stress vector [12] which is in the basal tangential direction, \mathbf{T}_{ti}^{n+1} . The magnitude of \mathbf{T}_{ti}^{n+1} is calculated based on the horizontal components $\tilde{\mathbf{q}}_i^{n+1} = (\tilde{q}_{x,i}^{n+1}, \tilde{q}_{y,i}^{n+1})$,

$$|\mathbf{T}_{ti}^{n+1}| = \frac{1}{\Delta t} \sqrt{|\tilde{\mathbf{q}}_i^{n+1}|^2 + \left(\tilde{q}_{x,i}^{n+1} \frac{\partial b}{\partial x} + \tilde{q}_{y,i}^{n+1} \frac{\partial b}{\partial y} \right)^2}. \tag{52}$$

The special procedure is as follows.

- 1) If the magnitude of the net driving force \mathbf{T}_t is less than the Coulomb threshold τ_{\max} , and the tilt angle of the free surface is less than the internal friction angle, i.e.,

$$|\mathbf{T}_{ti}^{n+1}| < \beta g' h_i^{n+1/2} \tan \phi_{\text{bed}}, \text{ and } |\nabla(h_i^{n+1/2} + b)| < \tan \phi_{\text{int}}, \tag{53}$$

then the local mass stops, $\mathbf{q}_i^{n+1} = 0$. Actual values of $\mathbf{f}_i^{n+1/2}$ are not needed.

- 2) Otherwise, the momentums \mathbf{q}_i^{n+1} are computed using scheme (50) with the friction force $\mathbf{f}_i^{n+1/2}$ evaluated with dynamic values as given in Eq. 46. The dynamic quantity $(u, v)_i^{n+1/2}/|\mathbf{v}_{ri}^{n+1/2}|$ in Eq. 46 is replaced by $(\tilde{q}_x, \tilde{q}_y)_i^{n+1}/|\mathbf{T}_{ti}^{n+1}|\Delta t$ when $|\mathbf{u}_i^{n+1/2}| \leq \varepsilon_{\text{tol}} = 10^{-6}$ to avoid division by zero.

6 Numerical examples

The present simplified model is implemented in TITAN2D code and tested in a dam break problem having an analytical solution, an avalanche problem over simple topography, and a granular avalanche problem in the laboratory. For convenience of discussion, we refer to model A as governing Eq. 44 with g' being (42), model B as Eq. 44 with g' being Eq. 10 but $\partial \bar{w}/\partial t$ is set zero to make the model run stably, and model C as Eq. 44 with $g' = 9.8 \text{ m/s}^2$, $\beta = \Delta_b = 1$, $(u, v)/|\mathbf{v}_r| \rightarrow (u, v)/|\mathbf{u}|$. All the models use $k_x = k_y = 1$ except stated explicitly in Fig. 7e. Actually, model C is the conventional Saint-Venant equations in the horizontal Cartesian coordinate system except having additional lateral shear stress terms as in Eq. 46.

Determination of friction angles is a big problem in realistic applications. Friction angles depend on many factors like granular and basal material types, even flow variables and shear rates. Friction angles are often obtained from experiments. Refs. [9, 10] gave variable friction angles dependent on Froude number and flow height which seem to be a better choice than constant friction angles. In this paper, we adopt the same constant friction angles as given in the literature for comparison purpose.

6.1 Analytical solution of dam break problem

Mangeney et al. [40] gave the analytical solution for a one-dimensional dam break problem over an inclined plane in terms of thickness \tilde{h} normal to the bed and coordinate \tilde{x} tangential to the bed. Juez et al. [38] obtained the analytical solution for a similar dam break problem but in terms of vertical thickness h and horizontal coordinate x . We compare our calculation with the analytical solution [38] since both

solutions are expressed in the same horizontal coordinate system.

The considered problem is an inclined plane, on which a granular mass of a constant thickness and infinite length in the positive x direction is released from rest. Let θ be the constant slope angle ($\theta > \phi_{\text{bed}}$) and u the horizontal velocity. For this slope, $\partial_x b = \tan \theta$. Assuming g' is constant and $\phi_{\text{int}} = 0$, $\beta = 1$, Eq. 44 reduces to

$$\begin{aligned} \frac{\partial h}{\partial t} + u \frac{\partial h}{\partial x} + h \frac{\partial u}{\partial x} &= 0, \\ \frac{\partial u}{\partial t} + u \frac{\partial u}{\partial x} + g' \frac{\partial h}{\partial x} &= -g'(\tan \theta - \tan \phi_{\text{bed}}). \end{aligned} \tag{54}$$

Juez et al. [38] took $g' = g \cos^2 \theta$ to obtain the analytical solution. Denoting $m = -g'(\tan \theta - \tan \phi_{\text{bed}})$ and using the following change of variables [40],

$$\begin{aligned} \chi &= x - \frac{1}{2} m t^2, \quad \tau = t, \\ \mathcal{U} &= u - m t, \quad \mathcal{H} = h, \end{aligned} \tag{55}$$

Equation 54 can be transformed into a homogeneous system of equations for a frictionless, horizontal dam break problem with gravity acceleration of g' , of which the classic Ritter solution [41] gives

$$(h, u) = \begin{cases} (h_0, m t), & \chi > c_0 t \\ \left(\frac{h_0}{9} \left(2 + \frac{\chi}{c_0 t} \right)^2, \frac{2}{3} \left(\frac{\chi}{t} - c_0 \right) + m t \right), & -2c_0 t \leq \chi \leq c_0 t \\ (0, \text{arbitrary value}), & \chi < -2c_0 t \end{cases} \tag{56}$$

where $c_0 = \sqrt{g' h_0}$, and h_0 is the initial upstream vertical thickness.

We compare our numerical results with the analytical solution (56). The computational domain is $[-1000, 1000] \times [-250, 250] \text{ m}^2$ and is partitioned with 1024×256 uniform meshes. $g = 9.8 \text{ m/s}^2$. Figure 3 depicts the comparison between the numerical solutions for two different values of the bed friction angle and bed slope and the analytical solutions.

In Fig. 3a, with bed slope angle $\theta = 0$ and friction angles $\phi_{\text{bed}} = \phi_{\text{int}} = 0$, a granular mass of 20 m high, infinitely long in the positive x -direction on a flat bottom is suddenly released. It can be seen that all the three models produce the same results in good agreement with the analytical solution. In the situation of a perfectly horizontal bottom, model A is the same as model C since Eq. 42 gives $g'_A = g$ and Eq. 30 gives $\beta = 1$. For model B, since \bar{w} is varying in the rarefaction zone, $D\bar{w}/Dt$ is nonzero as seen from Eqs. 11–12, causing $g'_B \neq g$. Anyway, the numerical result has no noticeable difference from those obtained by models A and C.

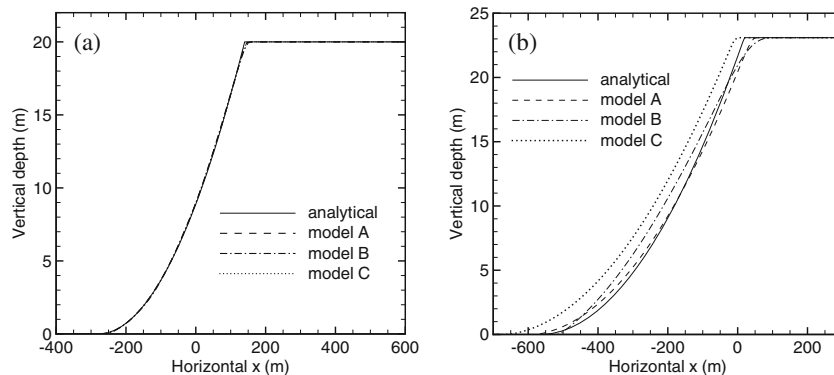


Fig. 3 Comparison of computed flow depth in the vertical direction versus horizontal distance from the initial edge of the dam at $x = 0$ with the analytical solution. **a** Results for a tabular reservoir of sand with zero bed slope, zero internal friction, and zero bed friction at

$t = 10$ s. **b** Results for a tabular reservoir of sand with a 30° bed slope, zero internal friction, and 20° basal friction at $t = 15$ s. Meanings of models A, B, and C are explained in the beginning of Section 6

In Fig. 3b with $\theta = 30^\circ$, $\phi_{bed} = 20^\circ$ and $\phi_{int} = 0^\circ$, a tabular reservoir of sand of $20/\cos\theta$ m high in the vertical direction on the inclined slope is released from the initial position at $x = 0$ and the flow depth is shown at $t = 15$ s. It can be seen that the result of model A is closer to the analytical solution than models B and C. Particularly, the avalanche motion predicted by model C is the quickest and deviates most from the analytical solution.

The reason why model C gives quicker avalanche can be explained as follows. From the momentum component of Eq. 54, the driving force is

$$F_x = -g'(\tan\theta - \tan\phi_{bed}) - g' \frac{\partial h}{\partial x}. \tag{57}$$

Since $(\tan\theta - \tan\phi_{bed}) > 0$ and $\partial h/\partial x > 0$ in the whole domain, it is evident that larger g' has larger driving force to the negative x direction, making the sand collapse faster. Thus, for model C, since $g'_C = g > g \cos^2\theta$, the computed avalanche flow will be faster than the analytical solution.

For models A and B, since g' depends on the solution, it is difficult to analyze the motion generally. However, model A can be analyzed here. Equation 42 for this problem gives

$$g'_A = \left(\frac{1 + \tan\theta \tan\phi_{bed}}{1 + \tan\theta \cos^2\theta \frac{\partial h}{\partial x}} \right) g \cos^2\theta. \tag{58}$$

Depending on whether $\cos^2\theta(\partial h/\partial x) \geq \tan\phi_{bed}$ in different locations, g'_A can be smaller or larger than $g \cos^2\theta$, making the computed avalanche motion lag behind or precede the analytical solution in different locations as shown in Fig. 3(b).

6.2 One-dimensional granular avalanche over simplified topography

The granular avalanches over a simple transversally uniform 2-D topography [28] is chosen here to illustrate the performances of various models. The elevation of this topography decreases from $b = 0$ m at $\tilde{x} = x = 0$ m in the left end with a maximum slope inclination of 35° to $b \approx -985.9$ m at $\tilde{x} = 5000$ m in the right end with slope inclination of about 2 degrees, where \tilde{x} is a bed-fitted coordinate tangential to the basal surface, and x is the global horizontal Cartesian coordinate. The corresponding bed slope angle and curvature are defined by

$$\theta(\tilde{x}) = \theta_0 \exp\left(-\frac{\tilde{x}}{a}\right), \quad \kappa = -\frac{d\theta}{d\tilde{x}} = \frac{\theta(\tilde{x})}{a}, \tag{59}$$

with $\theta_0 = 35^\circ$, $a = 1750$ m. The topography shape $z_b = b(x)$ is parameterized with the local coordinate \tilde{x} via following relations

$$\frac{db}{d\tilde{x}} = -\sin(\theta(\tilde{x})), \quad \frac{dx}{d\tilde{x}} = \cos(\theta(\tilde{x})). \tag{60}$$

With the starting point chosen as $b = 0, x = 0$ at $\tilde{x} = 0$, the topography shape can be integrated numerically. The solid curve in Fig. 4 shows the bed topography in the global Cartesian coordinates (x, z) .

The dashed curve in Fig. 4 depicts the initial parabolic shape of a pile over the topography represented in the bed-fitted coordinate. The initial conditions of the flow are defined by the instantaneous release of the granular mass,

$$\begin{aligned} \tilde{h}(\tilde{x}, t = 0) &= K \left[l - (\tilde{x} - \tilde{x}_0)^2 \right], \\ \tilde{u}(\tilde{x}, t = 0) &= 0, \end{aligned} \tag{61}$$

where $K = 1.25 \times 10^{-3} \text{ m}^{-1}$, $l = 1.6 \times 10^5 \text{ m}^2$, and $\tilde{x}_0 = 500$ m. Initially, the maximal thickness of the mass is 200 m in the basal normal direction with a length of 800 m

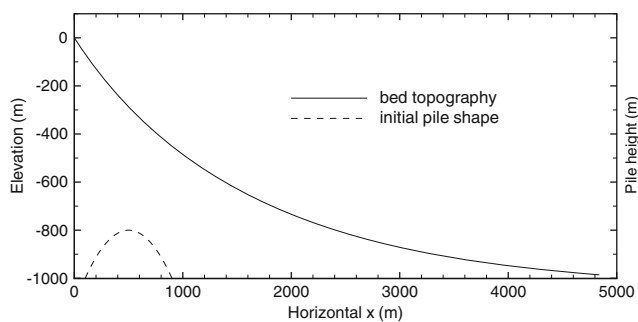


Fig. 4 Bed topography in the horizontal Cartesian coordinates (x, z) and initial shape of the granular mass in the topography-linked coordinates (\tilde{x}, \tilde{z})

in the tangential direction. In the horizontal Cartesian coordinate system, the initial shape is the same parabolic shape centered at the projected position of \tilde{x}_0 and imposed on the topography in the vertical z direction.

We simulate this problem by using Cartesian models A, B, and C and the SH model in the bed-fitted curvilinear coordinate system [30]. The solution domain is $[0, 5000] \times [0, 1250] \text{ m}^2$ for the bed-fitted model, and $[-100, 4840] \times [0, 1235] \text{ m}^2$ for the Cartesian models. The computational meshes used have the same 512 cells in the streamwise direction and 128 cells in transverse direction in both coordinate systems.

Figure 5 shows comparison of the calculated results between global Cartesian and bed-fitted models with $\phi_{\text{int}} = \phi_{\text{bed}} = 15^\circ$. Various models produced different results of which models A and B are in better agreement with the bed-fitted results than model C, while model C gives the fastest avalanches. The granular mass completely stops at $t = 87, 85$ and 82 s for models A, B, and C, respectively, and at $t = 86.5 \text{ s}$ for the bed-fitted model. The maximum depth

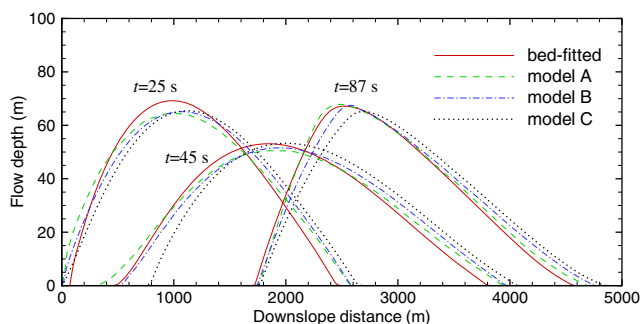


Fig. 5 Flow depth \tilde{h} vs. \tilde{x} on a simplified topography at $t = 25 \text{ s}$, 45 s , and 87 s ($t = 87 \text{ s}$ is when the granular mass stops for model A) computed by using various models for constant friction angles of $\phi_{\text{int}} = \phi_{\text{bed}} = 15^\circ$. The downslope distance is measured along the \tilde{x} direction on the topography. The flow depth \tilde{h} in the bed normal direction in models A, B, and C is approximated with Eq. 41. Meanings of models A, B, and C are explained in the beginning of Section 6

of the final deposit for model A is $\tilde{h}_{\text{max}} = 68.4 \text{ m}$, which is close to $\tilde{h}_{\text{max}} = 67.3 \text{ m}$ for the bed-fitted model. These data are also close to those ($t_{\text{stop}} = 86 \text{ s}$ and $\tilde{h}_{\text{max}} = 68 \text{ m}$) calculated in Ref. [28] using a topography-linked coordinate model. However, as different definitions in “flow depth” and “depth-averaged velocity” exist between the global Cartesian and the bed-fitted models, these intrinsic differences lead to different equations, thus quantitative differences between the global Cartesian and the bed-fitted models are expectable. In general, the downstream flow front predicted by the Cartesian models propagates faster than the bed-fitted model.

6.3 Avalanche over an inclined plane merging continuously into a horizontal plane

In this subsection we present a simulation example of an avalanche of finite granular mass sliding down an inclined plane and merging continuously into a horizontal plane [30]. The problem scales are nondimensional. A paraboloid of rotation holding the material together is suddenly released so that the bulk material commences to slide on an inclined flat plane at 35° into a horizontal run-out plane connected by a smooth transition. For the simulation using the body-fitted coordinates (\tilde{x}, \tilde{y}) , the computational domain is the rectangle $\tilde{x} \in [0, 30]$ and $\tilde{y} \in [-7, 7]$ in dimensionless length units, where the inclined section lies in the interval $\tilde{x} \in [0, 17.5]$ and the horizontal section lies where $\tilde{x} \geq 21.5$ with a smooth change in the topography in the transition zone, $\tilde{x} \in [17.5, 21.5]$. The inclination angle is prescribed by

$$\zeta(\tilde{x}) = \begin{cases} \zeta_0, & 0 \leq \tilde{x} \leq 17.5, \\ \zeta_0 \left(1 - \frac{\tilde{x} - 17.5}{4}\right), & 17.5 < \tilde{x} < 21.5, \\ 0, & \tilde{x} \geq 21.5, \end{cases} \quad (62)$$

where $\zeta_0 = 35^\circ$. The friction angles $\phi_{\text{bed}} = \phi_{\text{int}} = 30^\circ$. A paraboloid of rotation with height of $h_0 = 1.60$ and radius of $r_0 = 2.3$ centered at $(\tilde{x}_0, \tilde{y}_0) = (4, 0)$ is released suddenly at $t = 0$, see Fig. 6a. The initial vertical height in the horizontal coordinates can be calculated by rotation of coordinates around the center $(\tilde{x}_0, \tilde{y}_0) = (4, 0)$ with angle ζ_0 .

Figure 6b-d illustrate comparison of the thickness contours of the avalanche body at three time instants ($t = 9, 15$ and 24) as the avalanche slides on the inclined plane into the horizontal run-out zone. The results obtained by using different global Cartesian models are compared with those obtained by using the bed-fitted model [30]. Comparing Fig. 6b,c and d, it is seen that the avalanche speed increases from model A to model C, and all the Cartesian models produce quicker avalanche than the bed-fitted model. This difference may be attributed to intrinsic differences

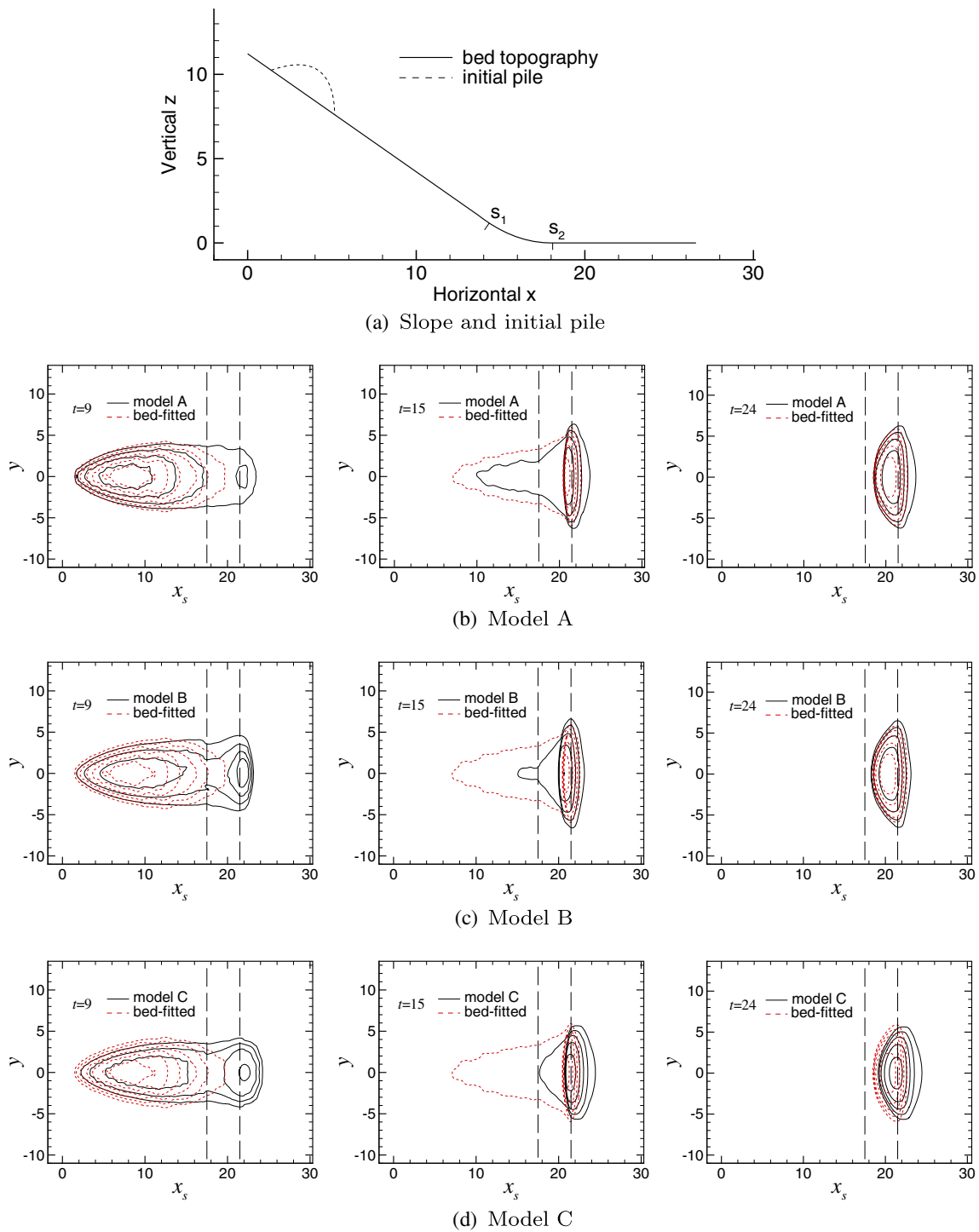


Fig. 6 **a** Side view of the bed topography and initial pile. The transition zone from the inclined plane to the horizontal plane lies for $S_1 = 17.5 < x_s < S_2 = 21.5$, where x_s is along the downslope direction. **b, c, d** Comparison of avalanche thickness contours at times $t = 9, 15$, and 24 computed with three Cartesian models and the

bed-fitted model [30]. Five equal contours from $h = 0.05$ to respective maximal depth in each frame are displayed. The zone between two long dashed lines is the transition zone. Meanings of models A, B, and C are given in the beginning of Section 6

in models such as different depth-averaging directions, as explained in the end of last subsection. The results of model A are in better agreement with the bed-fitted results. It is

observed that a shock wave develops just upstream of $x_s = 21.5$ at $t = 15$. With the arrival of mass from the tail, the shock wave propagates backwards. At $t = 15$, the position

of the shock in model A is almost coincident with that of the bed-fitted model, the shock in model B is more upstream, while the shock in model C is more downstream probably due to shock forming at more downstream position. At $t = 24$, the shock front almost reaches the beginning of the transition zone at $x_s = 17.5$ for the A, B, and bed-fitted models, and the final depositions of them are comparable. However, the deposition in model C is more downstream than that in the bed-fitted model.

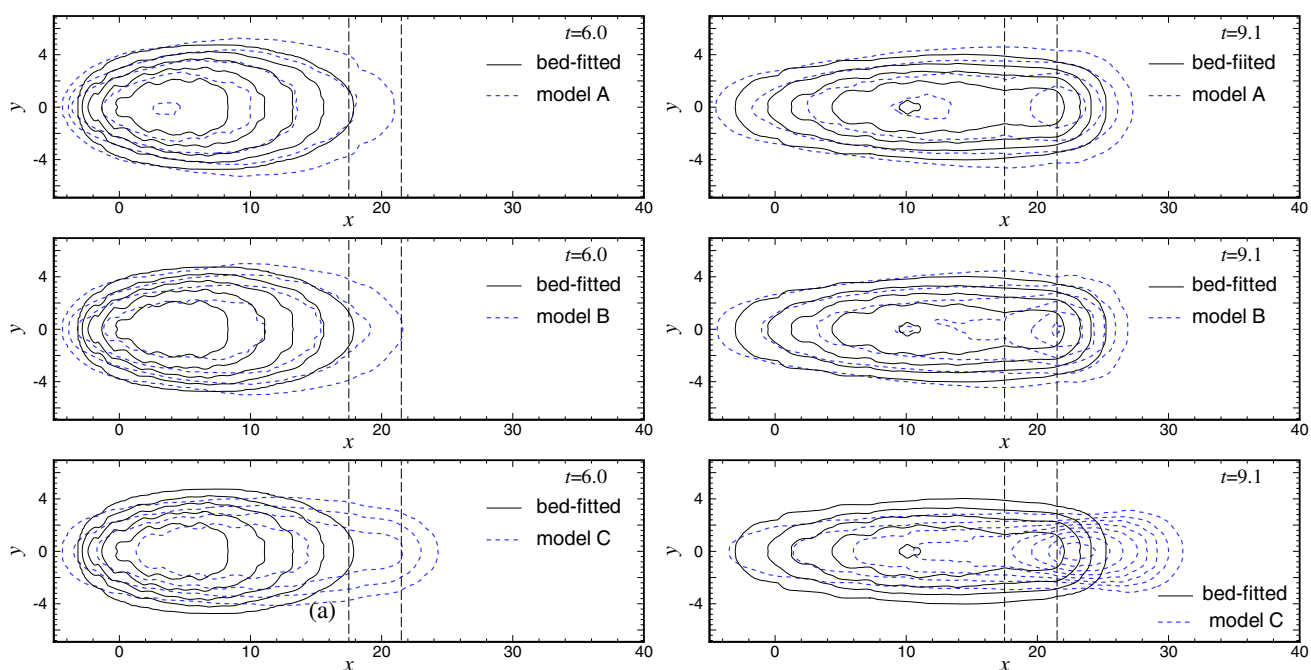
6.4 Granular avalanches in a chute with shallow lateral curvature

This example was taken from Wieland et al. [7] on the rapid fluid-like flow of a finite mass of granular material down

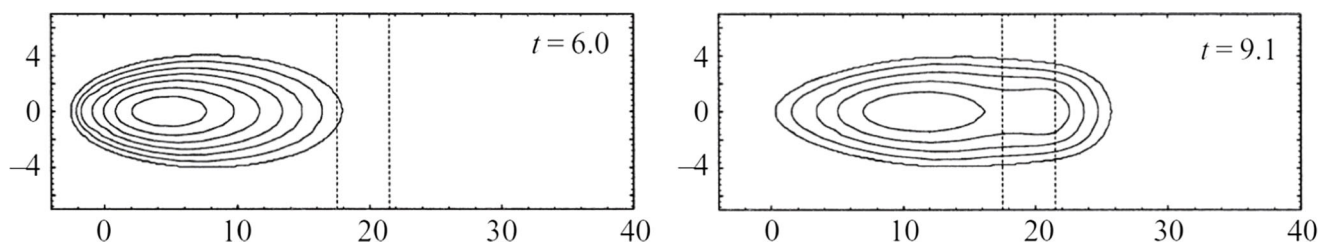
a chute with partial lateral confinement. The chute consists of a section inclined at 40° to the horizontal, which is connected to a plane run-out zone by a smooth transition. The reference surface is defined by the variation of its inclination angle, ζ , with the downslope coordinate x . The inclination angle of the reference plane is prescribed by

$$\zeta(x) = \begin{cases} \zeta_0, & x < x_a, \\ \zeta_0 \frac{x_b - x}{x_b - x_a}, & x_a \leq x \leq x_b, \\ 0, & x_b < x. \end{cases} \quad (63)$$

where $\zeta_0 = 40^\circ$, and $x_a = 175$ cm is the beginning of the transition zone and $x_b = 215$ cm is the end of the transition region. The side view of the reference plane is similar to the slope in Fig. 6a.



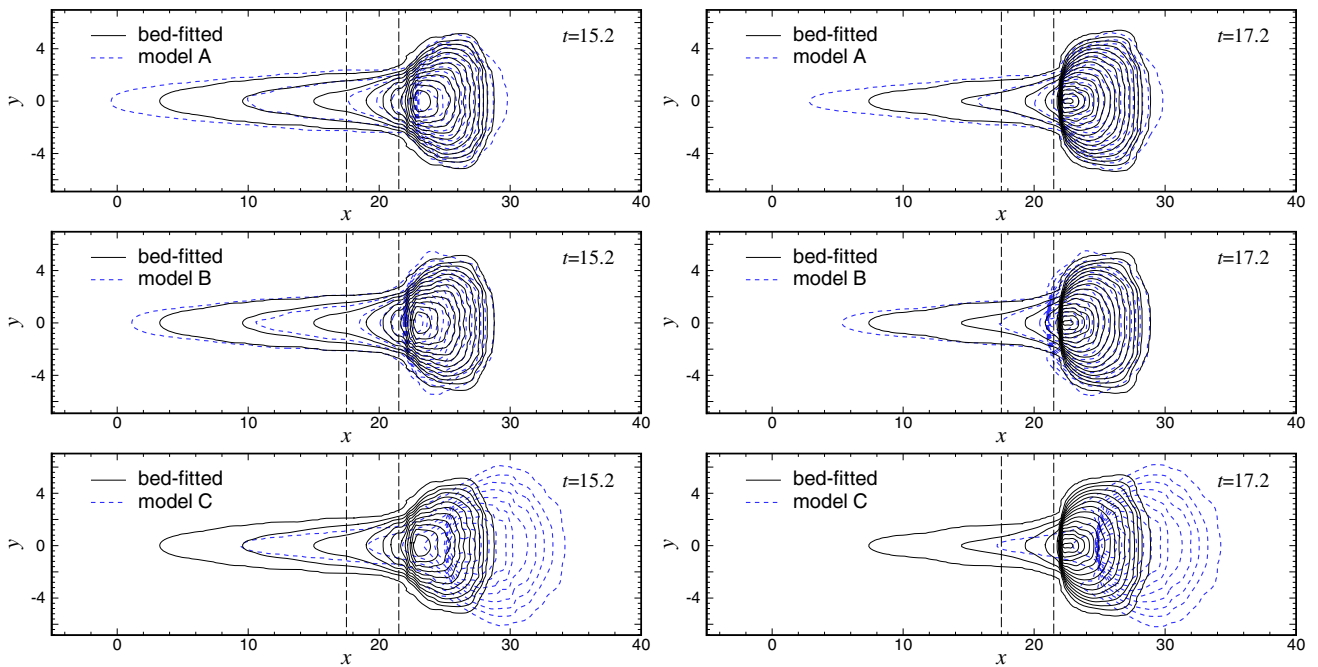
(a) Present results computed with $k_{ap} = 1$ at $t = 6$ and $t = 9.1$



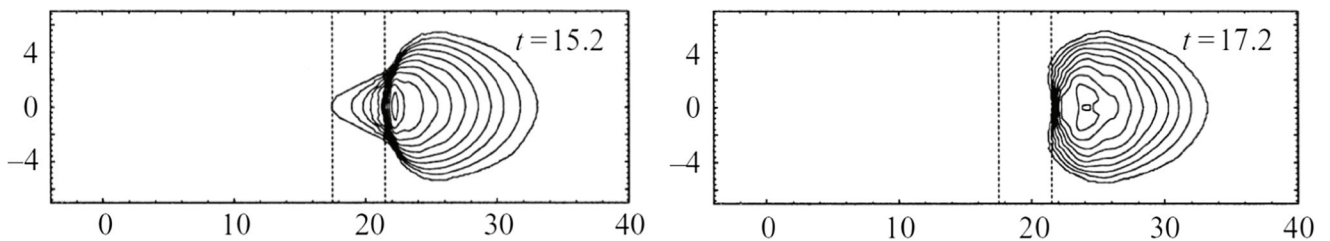
(b) Numerical results computed by Wieland *et al.* [7] with $k_{ap} \neq 1$ at $t = 6$ and $t = 9.1$

Fig. 7 Comparison of the present dimensionless avalanche thickness with the numerical and experimental results for experiment “V05” in Ref. [7]. The “bed-fitted” results are obtained by solving the conservative governing equations [30] (equivalent to the non-conservative form [7]) with the present finite volume scheme. The contour levels start from pile edge (at which the flow thickness is defined as 0.1 mm,

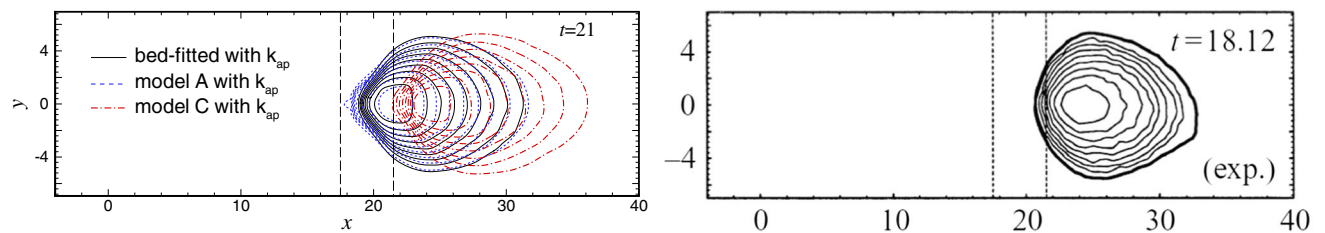
equivalent to 10^{-3} dimensionless unit) with 0.1 unit intervals. The zone between two long dashed lines is the transition zone. Meanings of models A, B, and C are given in the beginning of Section 6. Isotropic earth pressure coefficients $k_{ap} = 1$ are used in panels (a) and (c), while the coefficients $k_{ap} \neq 1$ [5] are used in panel (e)—*left*. (b) and (d) are numerical results computed by Wieland *et al.* [7]



(c) Present results computed with $k_{ap} = 1$ at $t = 15.2$ and $t = 17.2$



(d) Numerical results computed by Wieland *et al.* [7] with $k_{ap} \neq 1$ at $t = 15.2$ and $t = 17.2$



(e) Present results (left) and experimental result of Wieland *et al.* [7] (right)

Fig. 7 (continued)

As described in [7], the three-dimensional basal topography is superposed normal to the reference surface. A shallow parabolic cross-slope profile with radius of curvature $R = 110$ cm is prescribed on the inclined section of the chute, $x < x_a = 175$ cm. It opens out into a flat run-out zone in the region, $x > x_b = 215$ cm, and in the transition zone, $x_a \leq x \leq x_b$, a continuous differentiable function is constructed to provide a smooth change in the topography.

The function of the chute topography above the reference plane, $b(x, y)$, is

$$b(x, y) = \begin{cases} \frac{y^2}{2R}, & x < x_a, \\ \frac{y^2}{2R} \left[3 \left(\frac{x_b - x}{x_b - x_a} \right)^2 - 2 \left(\frac{x_b - x}{x_b - x_a} \right)^3 \right], & x_a \leq x \leq x_b, \\ 0, & x_b < x. \end{cases} \quad (64)$$

The initial condition of the flow is the granular material packed in a hemispherical cap centered at $(x_0, y_0, z_0) = (6, 0, -(r - h_c))$ cm, which is on the parabolic cross-slope basal topography. Here, r is the radius of the hemisphere and h_c is the maximum height of the initial free surface above the chute. The initial free surface, $s(x, y)$, of the granular material is described in the curvilinear reference coordinate system as

$$s(x, y) = \sqrt{r^2 - x^2 - y^2} - (r - h_c). \quad (65)$$

The projection of the intersection of the pile edge with the basal topology onto the $z = 0$ plane is approximately elliptical in shape. The major axis of the cap $r_b = 32$ cm, and the maximum height, $h_c = 22$ cm. The radius r is then determined by the relation $r^2 = r_b^2 + (r - h_c)^2$. The pile is released from rest.

We simulate experiment V05 in Ref. [7]. The granular material is plastic beads, and we use the same fixed basal angle of friction $\phi_{\text{bed}} = 27^\circ$ and internal angle of friction $\phi_{\text{int}} = 33^\circ$ as given in [7]. The computational domain is $[-50, 400] \times [-70, 70]$ cm² in the reference plane for the “bed-fitted” model computation, and is slightly extended in the horizontal x direction for the Cartesian model computation. A grid with 256×96 mesh cells is used in both coordinates.

Figure 7 illustrates comparisons of the computed thickness at several dimensionless times with the results [7]. The x and y coordinates in the reference plane are nondimensionalized with $L_{\text{ref}} = 10$ cm, and 0.1 unit intervals in thickness equal to 1 cm. The “bed-fitted” model we used is the conservative equations written in the orthogonal curvilinear coordinate system on the reference plane [30] (Eq. 63) that are reformulated from the Lagrangian form [7], and the equations are solved with the present finite volume scheme. Comparing Fig. 7a and b, we see that the present bed-fitted results at $t = 6.0$ and $t = 9.1$ are close to the Lagrangian numerical results [7]. But all the three Cartesian models produce quicker avalanche nose and slower tail compared with the present bed-fitted model, and results of models A and B are closer to the bed-fitted results than model C. Comparing panels c and d in Fig. 7, we can see that the shock wave in the present results begins to form at $t = 15.2$, and becomes strong at $t = 17.2$, while the numerical results [7] have a stronger shock wave at $t = 15.2$, and it propagates upslope and becomes weak at $t = 17.2$. Again, we see results of models A and B are closer to the bed-fitted results than model C. In Fig. 7e, we compare our deposited avalanche thickness distributions with the final avalanche deposit in experiment V05. For this panel we used the same

earth pressure coefficients $k_{\text{ap}} \neq 1$ as given in Refs. [5, 7]. It is seen that the result of model A (or B though not shown here) is very close to the bed-fitted one, while model C predicts a deposit at a more downstream position. The tail of the final deposit at $t = 21$ computed by model A and the present “bed-fitted” model is more upstream compared with the experimental result, yet the computed front and span extent are comparable to the experimental results.

7 Conclusions

Based on the non-hydrostatic shallow granular theory in the horizontal Cartesian system due to Castro-Orgaz et al. [2], we simplify the original expression of the vertical normal stress, and obtain a new formula for the basal normal stress by using the relationship between the vertical component of the basal traction vector integrated from the z -momentum equation and that of the basal Coulomb friction law. Together with some stress relations, we turn Castro-Orgaz et al.’s theory into a refined full non-hydrostatic shallow granular flow model in the horizontal Cartesian coordinate system. The equations are further rewritten in a form of Boussinesq-type water wave equations presumed more convenient for future numerical solution using numerical methods developed in water wave field.

In aid of numerical solution of a low-order version of the full non-hydrostatic model, we propose an approximate formula for the enhanced gravity based on the hypothesis of hydrostatic pressure in the bed normal direction and the Taylor expansion. Correspondingly, we add a “centripetal normal stress” due to the curvature tensor to the basal normal stress in the RHS terms. The resulting simplified shallow granular flow model is implemented in the open-source code TITAN2D for simulating granular flows over arbitrary topography. A series of numerical examples were carried out to test the suitability of the simplified model. Numerical results for granular avalanches over simple topographies show that the simplified model can produce results comparable to those obtained with a topography-fitted formulation, while the Saint-Venant equations in the horizontal Cartesian coordinates produce inaccurate results for steep slopes. It is concluded that the present simplified model can be used to model shallow granular flows over steep terrains.

Acknowledgements L. Yuan, W. Liu, J. Zhai thank the support of state key program for developing basic sciences (2010CB731505, MJ-F-2012-04) and Natural Science Foundation of China (11321061, 11261160486, 91641107). S. Wu thanks the support of the Department of Education of Guangdong Province (2014KQNCX175). A. Patra and

E. Pitman acknowledge the support of NSF grants 0620991, 0757367, 0711497, 1228217, and NSF/OAC-1339765.

The modified TITAN2D code can be downloaded from <http://lsec.cc.ac.cn/~lyuan/code.html>.

References

- Denlinger, R.P., Iverson, R.M.: Granular avalanches across irregular three-dimensional terrain: 1. Theory and computation. *J. Geophys. Res.* **109**, F01014 (2004). doi:[10.1029/2003JF000085](https://doi.org/10.1029/2003JF000085)
- Castro-Orgaz, O., Hutter, K., Giraldez, J.V., Hager, W.H.: Non-hydrostatic granular flow over 3D terrain: new Boussinesq-type gravity waves?. *J. Geophys. Res. Earth Surf.*, **120**(1), doi:[10.1002/2014JF003279](https://doi.org/10.1002/2014JF003279) (2014)
- Pudasaini, S., Hutter, K.: *Avalanche dynamics: dynamics of rapid flows of dense granular avalanches*, p. 47. Springer-Verlag, Berlin (2007)
- Grigorian, S.S., Eglit, M.E., Yakimov, I.L.: A new formulation and solution of the problem of snow avalanche motion. *Snow, Avalanches & Glaciers. Tr. Vysokogorn. Geofiz. Inst.* **12**, 104–113 (1967)
- Savage, S., Hutter, K.: The motion of a finite mass of granular material down a rough incline. *J. Fluid Mech.* **199**, 177–215 (1989)
- Iverson, R.M.: The physics of debris flows. *Rev. Geophys.* **35**, 245–296 (1997)
- Wieland, M., Gray, J.M.N.T., Hutter, K.: Channelized free-surface flow of cohesionless granular avalanches in a chute with shallow lateral curvature. *J. Fluid Mech.* **392**, 73–100 (1999)
- Denlinger, R.P., Iverson, R.M.: Flow of variably fluidized granular masses across three-dimensional terrain: 2. Numerical predictions and experimental tests. *J. Geophys. Res.* **106**, 553–566 (2001)
- Pouliquen, O., Forterre, Y.: Friction law for dense granular flows: application to the motion of a mass down a rough inclined plane. *J. Fluid Mech.* **453**, 133–151 (2002)
- MiDi, G.D.R.: On dense granular flows. *Eur. Phys. J. E: Soft Matter* **14**(4), 341–365 (2004)
- Mangeney, A., Bouchut, F., Thomas, N., Vilotte, J.P., Bristeau, M.O.: Numerical modeling of self-channeling granular flows and of their levee-channel deposits. *J. Geophys. Res.* **112**, F02017 (2007). doi:[10.1029/2006JF000469](https://doi.org/10.1029/2006JF000469)
- Maeno, F., Hogg, A.J., Sparks, R.S., Matson, G.P.: Unconfined slumping of a granular mass on a slope. *Phys. Fluids* **25**, 023302 (2013). doi:[10.1063/1.4792707](https://doi.org/10.1063/1.4792707)
- McDougall, S., Pirulli, M., Hungr, O., Scavia, C.: Advances in landslide continuum dynamic modelling. In: *Proceedings of the Tenth International Symposium on Landslides and Engineered Slopes (Volume 1)*. Taylor and Francis Group, London, UK (2008)
- Luca, I., Hutter, K., Tai, Y.C., Kuo, C.Y.: A hierarchy of avalanche models on arbitrary topography. *Acta Mech.* **205**, 121–149 (2009)
- Kuo, C., Tai, Y.C., Bouchut, F., Mangeney, A., Pelanti, M., Chen, R., Chang, K.: Simulation of Tsaoling landslide, Taiwan, based on Saint Venant equations over general topography. *Engng Geol.* **104**(3–4), 181–189 (2009)
- Takahashi, T., Nakagawa, H., Harada, T., Yamashiki Y.: Routing debris flows with particle segregation. *J. Hydr. Res.* **118**(11), 1490–1507 (1992)
- Wu, J., Chen, G.Q., Zhang, L., Zhang, Y.B.: GIS-Based numerical modelling of debris flow motion across three-dimensional terrain. *J. Mt. Sci.* **10**(4), 522–531 (2013)
- Patra, A.K., Bauer, A.C., Nichita, C.C., Pitman, E.B., et al.: Parallel adaptive numerical simulation of dry avalanches over natural terrain. *J. Volcanol. Geotherm. Res.* **139**(1), 1–21 (2005)
- Chau, K.T., Lo, K.H.: Hazard assessment of debris flows for Leung King estate of Hong Kong by incorporating GIS with numerical simulations. *Nat. Hazards Earth Syst. Sci.* **4**, 103–116 (2004). doi:[10.5194/nhess-4-103-2004](https://doi.org/10.5194/nhess-4-103-2004)
- Hergarten, S., Robl, J.: Modelling rapid mass movements using the shallow water equations in Cartesian coordinates. *Nat. Hazards Earth Syst. Sci.* **15**, 671–685 (2015). doi:[10.5194/nhess-15-671-2015](https://doi.org/10.5194/nhess-15-671-2015)
- Gray, J.M.N.T., Wieland, M., Hutter, K.: Free surface flow of cohesionless granular avalanches over complex basal topography. *Proc. Roy. Soc. London A* **455**, 1841–1874 (1999)
- Pudasaini, S., Hutter, K., Eckart, W.: Gravity-driven rapid shear flows of dry granular masses in topographies with orthogonal and non-orthogonal metrics. In: Hutter, K., Kirchner, N. (eds.) *Dynamic response of granular and porous materials under large and catastrophic deformation. Lecture Notes in Applied and Computational Mechanics*, vol. 11, pp. 43–82. Springer, Berlin (2003)
- Bouchut, F., Mangeney-Castelnau, A., Perthame, B., Vilotte, J.P.: A new model of Saint-Venant and Savage-Hutter type for gravity driven shallow water flows. *C. R. Acad. Sci. Paris Ser. I* **336**, 531–536 (2003)
- Bouchut, F., Westdickenberg, M.: Gravity driven shallow water models for arbitrary topography. *Commun. Math. Sci.* **2**(3), 359–389 (2004)
- Green, A., Naghdi, P.: A derivation of equations for wave propagation in water of variable depth. *J. Fluid Mech.* **78**, 237–246 (1976)
- Bristeau, M.-O., Mangeney, A., Sainte-Marie, J., Seguin, N.: An energy-consistent depth-averaged Euler system: derivation and properties. *Discret. Contin. Dyn. Syst. Ser. B* **20**(4), 961–988 (2015). doi:[10.3934/dcdsb.2015.20.961](https://doi.org/10.3934/dcdsb.2015.20.961)
- Gray, J.M.N.T.: Rapid granular avalanches. In: Hutter, K., Kirchner, N. (eds.) *Dynamic response of granular and porous material under large and catastrophic deformations. Lecture Notes in Applied and Computational Mechanics*, vol. 11, pp. 3–42. Springer (2003)
- Mangeney-Castelnau, A., Vilotte, J.P., Bristeau, M.O., Perthame, B., Bouchut, F., Simeoni, C., Yerneni, S.: Numerical modeling of avalanches based on Saint Venant equations using a kinetic scheme. *J. Geophys. Res.* **108**(B11), 2527 (2003). doi:[10.1029/2002JB002024](https://doi.org/10.1029/2002JB002024)
- GMFG: Titan2d: A open-source simulation code for dry granular avalanche flow over natural terrain. <http://www.gmfg.buffalo.edu> (Unknown Month 2007)
- Wang, Y.Q., Hutter, K., Pudasaini, S.P.: The Savage-Hutter theory: A system of partial differential equations for avalanche flows of snow, debris, and mud. *Z. Angew. Math. Mech.* **84**(8), 507–527 (2004). doi:[10.1002/zamm.200310123](https://doi.org/10.1002/zamm.200310123)
- De Toni, S., Scotton, P.: Two-dimensional mathematical and numerical model for the dynamics of granular avalanches. *Cold. Reg. Sci. Tech.* **43**, 36–48 (2005)
- Kelfoun, K., Druitt, T.H.: Numerical modeling of the emplacement of Socompa rock avalanche, Chile. *J. Geophys. Res.* **110**, B12202 (2005)

33. Chen, W.-C., Kuo, C.Y., Shyue, K.M., Tai, Y.-C.: Gas kinetic scheme for anisotropic Savage-Hutter model. *Commun. Comput. Phys.* **13**(5), 1432–1454 (2013). doi:[10.4208/cicp.190112.250512a](https://doi.org/10.4208/cicp.190112.250512a)
34. Iverson, R.M., Denlinger, R.P.: Flow of variably fluidized granular masses across three-dimensional terrain: 1. Coulomb mixture theory. *J. Geophys. Res.* **106**, 537–552 (2001)
35. Kim, D.H., Lynett, P.J., Socolofsky, S.: A depth-integrated model for weakly dispersive, turbulent, and rotational fluid flows. *Oc. Model.* **27**(3-4), 198–214 (2009)
36. Fang, K.Z., Zhang, Z., Zou, Z., Liu, Z., Sun, J.W.: Modelling of 2-D extended Boussinesq equations using a hybrid numerical scheme. *J. Hydrodyn.* **26**(2), 187–198 (2014). doi:[10.1016/S1001-6058\(14\)60021-4](https://doi.org/10.1016/S1001-6058(14)60021-4)
37. Pitman, E.B., Le, L.: A two-fluid model for avalanche and debris flows. *Philos. Trans. R. Soc. A Math. Phys. Eng. Sci.* **363**(1832), 1573–1601 (2005)
38. Juez, C., Murillo, J., García-navarro, P.: 2D simulation of granular flow over irregular steep slopes using global and local coordinates. *J. Comput. Phys.* **255**, 166–204 (2013)
39. Davis, S.F.: Simplified second order Godunov type methods. *SIAM J. Sci. Statist. Comput.* **9**, 445–473 (1988)
40. Mangeney, A., Heinrich, P., Roche, R.: Analytical solution for testing debris avalanche numerical models. *Pure. Appl. Geophys.* **157**, 1081–1096 (2000)
41. Ritter, A.: Die Fortpflanzung der Wasserwelle. *Ver. Deutsch. Ing. Z.* **36**, 947–954 (1892)